JOURNAL OF GEOPHYSICAL RESEARCH: ATMOSPHERES, VOL. 118, 1–20, doi:10.1002/jgrd.50410, 2013

Precipitation intensity and variation during MC3E: A numerical modeling study

Wei-Kuo Tao,[1] Di Wu,[1,2] Toshihisa Matsui,[1,3] Christa Peters-Lidard,[4] Stephen Lang,[1,2] Arthur Hou,[1] Michele Rienecker,[5] Walter Petersen,[6] and Michael Jensen[7]

Received 16 November 2012; revised 25 February 2013; accepted 10 April 2013.

[1] Previous observational studies have identified three different types of diurnal precipitation variation over the conterminous U.S.: localized afternoon rainfall maxima over the Mississippi and Ohio valleys, propagating mesoscale convective systems (MCSs) from the Rocky Mountain region, and propagating MCSs over the Appalachian Mountains. This study focuses on the second type, which involves nocturnal rainfall maxima from eastward-propagating MCSs on the lee side of the Rocky Mountains. This study evaluates model simulations with regard to rainfall using observations and assesses the impact of microphysics, surface fluxes, radiation, and terrain on the simulated diurnal rainfall variation. A regional high-resolution model was used to conduct a series of real-time forecasts during the Midlatitude Continental Convective Clouds Experiment (MC3E) in 2011 over the Southern Great Plains. The model ably captured most heavy precipitation events. When all forecast days are composited, the mean forecast depicts accurate, propagating precipitation features and thus the overall diurnal variation. However, individual forecasts tend to overestimate the rainfall for light precipitation events, have location errors, and misrepresent convection in some cases. A post mission case study is performed on one multi-cell, eastward-propagating MCS event; the results suggest that cold-pool dynamics were an important physical process. Model results also indicate that terrain effects are important during the initial stages of MCS development. By increasing the terrain height by 10%, the simulated rainfall is increased and in better agreement with observations. On the other hand, surface fluxes, and radiation processes only have a secondary effect for short-term simulations.

Citation: Tao, W.-K., D. Wu, T. Matsui, C. Peters-Lidard, S. Lang, A. Hou, M. Rienecker, W. Peterson, and M. Jensen (2013), Precipitation intensity and variation during MC3E: A numerical modeling study, *J. Geophys. Res. Atmos.*, *118*, doi:10.1002/jgrd.50410.

1. Introduction

[2] The diurnal variation of precipitation processes in the United States (US) is well recognized but incompletely understood [*Carbone et al.*, 2002]. The diurnal cycle of precipitation has been studied using surface rainfall data, radar reflectivity data, and satellite-derived cloudiness and precipitation [*Wallace*, 1975; *Dai et al.*, 1999; *Carbone et al.*, 2002; *Carbone and Tuttle*, 2008; *Parker and Ahijevych*, 2007; *Matsui et al.*, 2010; and others]. These observations indicate that summertime precipitation over most of North America can be generally categorized into three different types: (1) an afternoon rainfall maximum due to mesoscale and local circulations south and east of the Mississippi and Ohio valleys, (2) nocturnal rainfall maxima from eastward-propagating MCSs in the lee of the Rocky Mountains, and (3) an afternoon rainfall maximum over the Appalachian Mountains that propagates eastward toward the coast.

[3] Regional-scale numerical models have been used to simulate the diurnal variation of precipitation processes over the US (Table 1). *Davis et al.* [2003] used two different models, the National Centers for Environmental Prediction (NCEP) Eta and Weather Research and Forecasting (WRF), with 12 and 22 km grid sizes and found that the diurnal cycle of summer (July to August in 2001 and 2002) rainfall over most of the United States east of the Rockies is poorly represented, particularly over the central US in association with eastward-propagating MCSs. Their results also showed that the diurnal cycle associated with

[1]Mesoscale Atmospheric Processes Laboratory, NASA Goddard Space Flight Center, Greenbelt, Maryland, USA.
[2]Science Systems and Applications, Inc., Lanham, Maryland, USA.
[3]Earth System Science Interdisciplinary Center, University of Maryland, College Park, Maryland, USA.
[4]Hydrological Sciences Laboratory, NASA Goddard Space Flight Center, Greenbelt, Maryland, USA.
[5]Global Modeling and Assimilation Office, NASA Goddard Space Flight Center, Greenbelt, Maryland, USA.
[6]NASA Wallops Flight Facility, Wallops Island, Virginia, USA.
[7]Brookhaven National Laboratory, Upton, NY, USA.

Corresponding author: W.-K. Tao, Code 612, NASA Goddard Space Flight Center, Greenbelt, MD 20771, USA. (Wei-Kuo.Tao-1@nasa.gov)

2169-897X/13/10.1002/jgrd.50410

Table 1. Key High-Resolution Modeling Papers on the Diurnal Variation of Precipitation[a]

	Model	Forcing Data	Physics	Domain Size	Resolution	Period
Moncrieff and Liu [2006]	MM5	Eta operational model analyses	Microphysics and cumulus parameterization	2400 × 1800 km	3 and 10 km 40 layers	7 day simulation 3–9 July 2003
Liu *et al*. [2006]						
Liang *et al*. [2004]	CMM5	NCEP-DOE Reanalysis	Grell Kain and Fritsch	North America	30 km	June, July, August 1982–2002
Surcel *et al*. [2010]	GEM	3DVAR regional Data Assimilation System	Kuo Kain and Fritsch	North America	15 km 58 layers	30 h forecast Spring and Summer 2008
Clark *et al*. [2007]	WRF-NMM WRF-ARW	NAM 12 km	Kain and Fritsch Ferrier	North Central US	5 km and 22 km 38 layers	48 h forecast 1 April–25 July, 2005
Davis *et al*. [2003]	Eta (NCEP) WRF	Eta forecast	Kain and Fritsch simple ice scheme	Continental United States (CONUS)	22 km	1–3 day forecast 2001 (July–August) and 2002 (June–July)
Trier *et al*. [2006]	WRF	Eta operational model analyses	Purdue-Lin	2500 × 1780 km	4 km	7 day simulation 3–10 July 2003
Trier *et al*. [2010]	WRF	Eta Monthly averaged	WSM6 [Hong et al. 2004]	2700 × 1800 km	3 km	10 days July 2001
Trier *et al*. [2011]	WRF	EDAS	Thompson	2400 × 2250 km	3 km	13 June, 2002
Lee *et al*. [2010]	GCE model	DOE ARM SGP	Goddard 3-Ice scheme	128 km	1 km 41 layers	55 days Summer 1995, 1997 and 1999

[a]Model types (i.e., MM5, WRF, GCE), microphysical schemes, cumulus parameterization, domain size (km), resolution (km), initial conditions, cases and integration time (hours) are listed. EDAS stands for the Environmental Data Assimilation System and CMM5 the MM5-based regional climate model.

localized non-propagating rainfall was reasonably represented in the regional model. Even in these areas, there is a characteristic bias in the timing of local convection in the Eta Model, which tends to occur several hours too early. They suggested that fundamental propagation errors result from using cumulus parameterizations in numerical weather prediction (NWP) models.

[4] *Clark et al*. [2007] used a convection-resolving 5 km grid-spacing and a non-convection-resolving 22 km grid-spacing configuration of the NCEP non-hydrostatic mesoscale model (NMM) to examine whether significant improvements could be obtained by using a grid spacing fine enough to explicitly resolve convection. The results showed that the representation in the diurnal cycle in the 5 km configuration is clearly superior to that in the 22 km configuration during forecast hours 24–48. This conclusion suggests that a convection-resolving resolution and explicit microphysics are required to better simulate the diurnal variation of precipitation processes. *Surcel et al*. [2010] used the Canadian Global Environmental Multiscale model (GEM) with uniform 15 km grid spacing over North America and found that GEM represented fairly well the timing of precipitation initiation along the Rockies during the 2008 spring and summer seasons. However, their results failed to capture the correct propagation characteristics of these systems. During spring, the simulated systems show more variability in propagation paths than observed, while during summer, the observed propagation was simply not captured by GEM. This is probably a consequence of different propagation mechanisms acting in the modeled atmosphere and between spring and summer. In spring, the combined effect of precipitation propagation (with a dominant west-east component) and the impact of solar heating on convective initiation/inhibition (happening earlier in the east than in the west) acting together result in rainfall peaks occurring at different times and at different locations. On the other hand, during the summer of 2008, GEM had no skill in reproducing the propagating signal in the western part of the domain. This result agreed with *Davis et al*. [2003] and *Clark et al*. [2007], who attributed this problem to the inability of the convective parameterization scheme to reproduce propagating convection that is phased locked with the diurnal cycle of solar heating.

[5] *Moncrieff and Liu* [2006] used the Fifth-Generation NCAR/Penn State Mesoscale Model (MM5) to demonstrate that a hybrid approach (i.e., explicit microphysics to represent mesoscale downdrafts and stratiform heating and cumulus parameterization to represent the propagating and dynamic structure of organized precipitating systems) can simulate the observed eastward propagation of organized convection originating in the lee of the Rockies under moderate large-scale forcing. They also suggested that the propagation of organized convection within the large-scale flow results in the diurnal variation of rainfall over the US. In addition, *Moncrieff and Liu* [2006] showed that the observed daily generation of convection near the Continental Divide and the subsequent propagation of organized convection are reproduced in the microphysics schemes. Their results suggested that mixed-phase microphysics schemes are superior to simple ice microphysics schemes. *Liu and Moncrieff* [2007] further suggested that the eastward propagation of organized convection is not sensitive to the choice of microphysics

schemes, but that upper-level radiative heating/cooling, cloudiness, and condensation, as well as the rainfall spectrum are sensitive to the microphysics schemes. *Liang et al*. [2004] used an MM5-based regional climate model (CMM5) with 30 km grid spacing and found that simulations of diurnal variation are sensitive to the choice of cumulus parameterization scheme. They showed that the Grell scheme can realistically simulate the nocturnal precipitation maxima and the associated eastward propagation of convective systems over the Great Plains where the diurnal timing of convection is controlled by large-scale tropospheric forcing. On the other hand, the Kain and Fritsch scheme was more accurate for the late afternoon peaks in the southeast US where moist convection is mainly influenced by near surface forcing.

[6] *Lee et al*. [2010] used the two-dimensional (2D) Goddard Cumulus Ensemble (GCE) cloud-resolving model to examine the mechanisms of summertime diurnal precipitation over the Great Plains. The model was constrained by the observed large-scale background state and surface fluxes derived from the Department of Energy (DOE) Atmospheric Radiation Measurement (ARM) Program's intensive observing period (IOP) data at the Southern Great Plains (SGP) site. The model was continuously forced by surface fluxes and large-scale advection. Sensitivity tests were conducted to discriminate between the mechanisms that determine daytime and nighttime convection. Their results indicate that surface heat and moisture fluxes are primarily responsible for the development of deep convection in the afternoon, whereas large-scale upward motion and associated moisture advection play an important role in preconditioning nocturnal convection. At night, high clouds are continuously built up through their interaction and feedback with long-wave radiation, eventually initiating deep convection from the boundary layer. Without these upper-level destabilization processes, the model tends to produce only daytime convection in response to boundary layer heating.

[7] *Trier et al*. [2006] used high-resolution (4 km grid spacing) in WRF to simulate eastward-traveling convection for a 1 week period during which regular long-lived episodes of deep convection attained maximum intensity and organization at night over the central United States. A multi-scale composite analysis of the environment and mesoscale convective structure of the multi-episode convection was then combined to determine the mechanisms responsible for the convective life cycle. Their results indicate that initial afternoon/early evening convection is based in the planetary boundary layer (PBL), but it is an elevated 2 km-deep layer of high-θ_e air that later helps to sustain the convection during its period of greatest organization (with squall-line characteristics) overnight. Trajectory analyses for individual episodes revealed that the high-θ_e air originated both from within and south of the frontal zone; in this latter case, it was transported northward by the nocturnal low-level jet (LLJ), a major source of moisture for the active convection regime. *Trier et al*. [2010] initialized WRF with monthly mean conditions common for midsummer and used time-varying lateral boundary conditions over the diurnal cycle. They were able to simulate the stationary afternoon precipitation frequency maximum over the Rocky Mountains and ensuing overnight eastward-progression of maximum precipitation frequencies within a narrow latitude band over the Great Plains. Their results suggest that progressive weather disturbances (e.g., mobile cold fronts and mid-tropospheric short waves) originating outside of the region may help enhance and focus precipitation in individual cases but are not crucial to the general location and diurnal cycle of midsummer precipitation. Their results also showed the importance of the nocturnal low-level jet and thermally induced mountain-plains vertical circulation on convection. Recently, *Trier et al*. [2011] used WRF to simulate a nocturnal MCS during IHOP_2002. Their results indicated the importance of environmental pre-conditioning with regard to MCS reorganization. A strong surface cold pool generated by the MCS is not a necessary condition for the reorganization and maintenance of the convection, but it can influence the strength and vertical structure of the MCS.

[8] Based on these numerical modeling and observational studies, the main physical processes that contribute to the diurnal variation of rainfall east of the Rockies generally are the following: (1) a large-scale flow containing an eastward upper-level wind component aloft [*Moncrieff and Liu*, 2006; *Carbone and Tuttle*, 2008; *Trier et al*., 2011; and others], (2) land surface (continental thermal) forcing including thermodynamic instability within the PBL [*Carbone et al*., 2002; *Lee et al*., 2007; *Trier et al*., 2006; *Carbone and Tuttle*, 2008], (3) successive propagating organized convection caused by convective gravity waves [*Tripoli and Cotton*, 1989a, 1989b; *Carbone et al*., 2002; *Moncrieff and Liu*, 2006; *Matsui et al*., 2010], (4) the transport of energetic air and moisture convergence by the Great Plains LLJ [*Trier et al*., 2006; *Carbone and Tuttle*, 2008], (5) a diabatic heating effect [*Moncrieff and Liu*, 2006], and (6) a nocturnal reversal of the mountain-plains solenoid, which is associated with widespread ascent over the plains [*Carbone et al*., 2002; *Carbone and Tuttle*, 2008].

[9] The main objective of this paper is to use a regional cloud-scale model with very high-resolution (i.e., the NASA Unified WRF or NU-WRF) to examine its ability to simulate the diurnal variation of precipitation associated with the propagation of organized convection observed during a major field campaign. Specifically, the study will (1) examine the model's ability to simulate the diurnal variation of rainfall, (2) identify the physical processes responsible for the diurnal variation of precipitation, and (3) examine the sensitivity of the simulated diurnal precipitation signal to terrain and surface and radiation effects. The simulations will also be compared with observations and previous modeling studies.

2. Model Setup and Case Descriptions

[10] Recently, several physical processes developed by NASA scientists have been implemented into WRF to better represent/simulate cloud-aerosol-precipitation-land surface processes on satellite-resolvable scales (~1 km grid spacing). These physical processes have been implemented into several WRF versions from 3.1.1 up through 3.4 and are collectively known as the NASA Unified WRF (NU-WRF). NU-WRF is available to non-NASA users. The NASA physical packages (microphysics, radiation) have also been implemented into the NCAR ARW (Advanced Research WRF). These physical

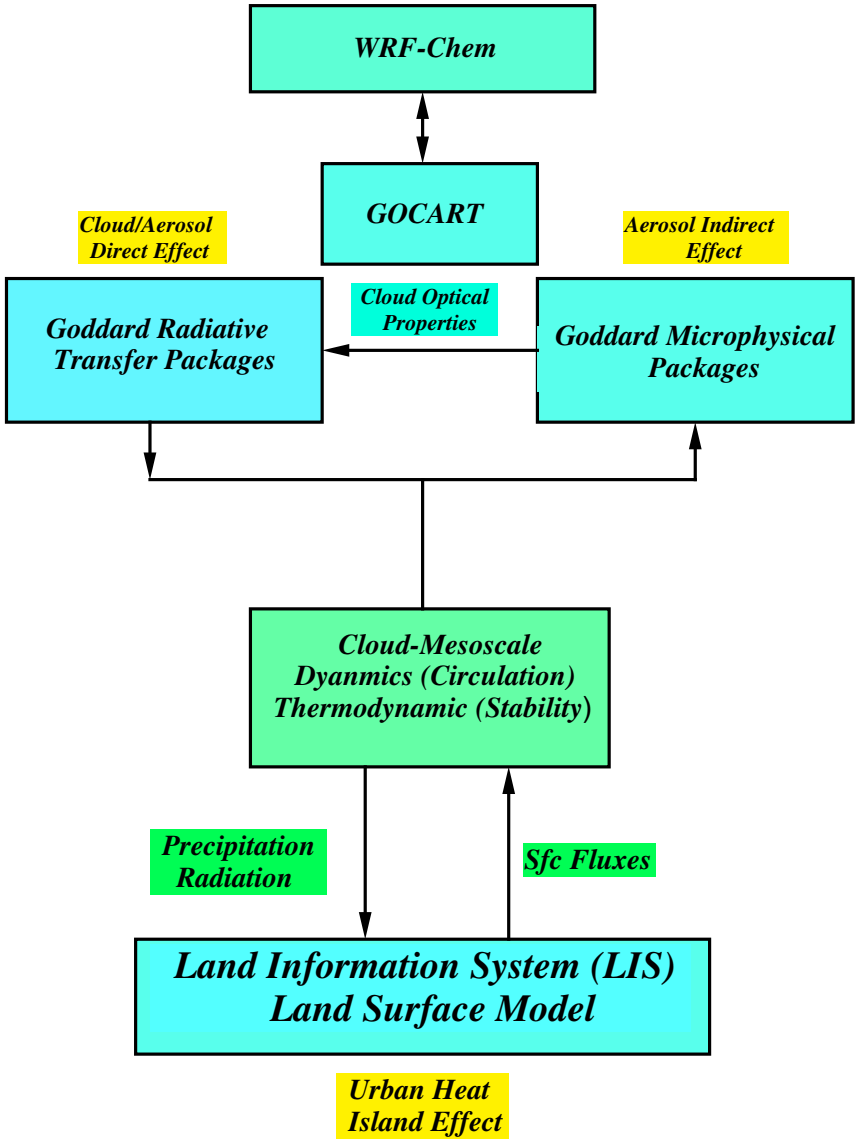

Figure 1. Schematic diagram showing planned components of the NASA Unified WRF. The blue boxes are the physical processes (packages) developed by NASA scientists. The light green boxes are the WRF dynamic core and others developed outside of NASA. GOCART stands for the Goddard Chemistry Aerosol Radiation and Transport model.

processes include CRM-based microphysics and CRM-based radiation (Figure 1) that have been tested on several convective systems in different environments, including a linear convective system in Oklahoma from the International H_2O project (IHOP-2002) [*Santanello et al.*, 2009], an Atlantic hurricane (Hurricane Katrina from 2005) [*Tao et al.*, 2011a], high latitude snow events from the Canadian CloudSat CALIPSO Validation Project (C3VP) in 2007 [*Shi et al.*, 2010; *Iguchi et al.*, 2012], and Typhoon Morakot in Taiwan from 2009 [*Tao et al.*, 2011b] as well as others. In addition, two other major NASA modeling components have been coupled with NU-WRF representing land surfaces (i.e., the Land Information System (LIS) [*Kumar et al.*, 2006, 2007]) and aerosols (i.e., the WRF Chemistry Model and Goddard Chemistry Aerosol Radiation and Transport Model (GOCART) [*Chin et al.*, 2000, 2002, 2004]).

2.1. Model Setup

[11] NU-WRF with improved microphysics that reduces unrealistically high dBZs aloft [*Lang et al.*, 2011] was used in this study. Figure 2 shows the model grid configuration, which includes an outer domain and two inner-nested domains, having 18, 6, and 2 km horizontal resolution and $213 \times 168 \times 61$, $277 \times 211 \times 61$, and $295 \times 235 \times 61$ grid points, respectively. Time steps of 18, 6, and 2 s were used in these nested grids, respectively. The Grell-Devenyi cumulus parameterization scheme [*Grell and Devenyi*, 2002] was used for the outer grid (18 km) only. For the inner two domains (6 and 2 km), the scheme was turned off. The PBL parameterization employed the Mellor-Yamada-Janjic [*Mellor and Yamada*, 1982] Level-2 turbulence closure model through the full range of atmospheric turbulent regimes. The Goddard broadband two-stream (upward and downward fluxes) approach was used for the short- and

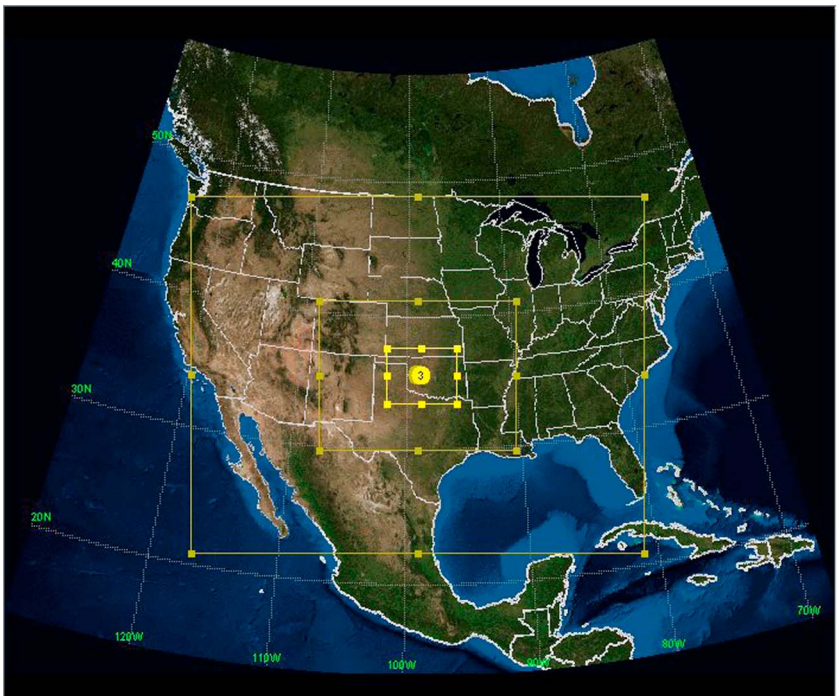

Figure 2. WRF nested domain configuration used for this study. The horizontal grid sizes are 18, 6, and 2 km for the outer, middle, and inner domains, respectively. The model terrain has a 2 km resolution and is smoothed from a 30 s (~0.9 km) terrain database.

long-wave radiative flux calculations [*Chou and Suarez*, 1999, 2001] and its explicit interactions with clouds (microphysics).

2.2. MC3E

[12] The Midlatitude Continental Convective Clouds Experiment (MC^3E) was a joint field campaign between the DOE ARM Climate Research Facility and NASA's Global Precipitation Measurement (GPM) mission Ground Validation (GV) program [*Petersen and Jensen*, 2012]. It took place in central Oklahoma from 22 April to 6 June 2011. Some of its major objectives involve the use of high-resolution cloud-resolving models (CRMs) in precipitation science and include the following: (1) testing the fidelity of CRM simulations via intensive statistical comparisons between simulated and observed cloud properties and latent heating (LH) fields for a variety of case types, (2) establishing the limits of CRM space-time integration capabilities for quantitative precipitation estimates, and (3) supporting the development and refinement of physically-based GPM microwave imager (GMI), dual-frequency precipitation radar (DPR), and DPR-GMI combined retrieval algorithms using ground-based observations,

Table 2. MC3E Precipitation Events Identified as Priority Cases for Post Mission Study

IOP#	Date	System	Forecast	Flight Duration
1	21Z April 22 to 08Z April 23	Squall line with leading stratiform	Accurate	ER2: 1919Z on 22nd to 0113Z on 23rd Citation: 2234Z on 22nd to 0057Z on 23rd
2	07Z April 25 to 12Z April 25	Scattered storms	12Z previous day location is off	ER2: 0712Z to 1246Z on 25th Citation: 0921Z to 1222Z on 25th
3	23Z April 26 to 15Z April 27	Scattered storms with stratiform	Location is a bit off, too much cloud	ER2: 0500Z to 1123Z on 27th Citation: 0802Z to 1123Z on 27th
4	09Z May 01 to 21Z May 01	Scattered storms with large stratiform coverage	Accurate	Citation: 1629Z–1842Z on 01st
5	19Z May 10 to 03Z May 11	Scattered storms with stratiform and mixed type precipitation	Location is a bit off, too much cloud	Citation: 2151Z on 10th to 0011Z on 11th
6	12Z May 11 to 00Z May 12	Squall line with trailing stratiform	00Z missed the event	ER2: 1505Z to 1923Z on 11th Citation: 1602Z to 1927Z on 11th
7	07Z May 18 to 15Z May 18	Squall line with leading stratiform	Accurate	ER2: 0512Z to 0955Z on 18th Citation: 0720Z to 0922Z on 18th
8	05Z May 20 to 06Z May 21	Squall line with extended trailing stratiform	19 12Z missed the event, 00Z doing OK	ER2: 1315Z to 1855Z on 20th Citation: 1306Z to 1702Z on 20th
9	20Z May 23 to 07Z May 24	Scattered storms	Accurate	ER2: 2055Z on 23rd to 0235Z on 24th Citation: 2130Z on 23rd to 0041Z on 24th
10	19Z May 24 to 05Z May 25	Squall line	00Z missed the event, 12Z good	Citation: 2018Z to 2228Z on 24th

Table 3. Sensitivity Tests Examining the Effect of Terrain Height, Surface Fluxes and Radiative Effects on the Diurnal Variation of Precipitation

Run	Terrain	Surface Fluxes	Radiation
WLIS	Yes	Yes	Yes
NOLIS	Yes	Yes	Yes
SFC1	Yes	No	Yes
SFC2	Yes	50%	Yes
Rad1	Yes	Yes	No
TRAN1	No	Yes	Yes
TRAN2	Half	Yes	Yes
TRAN3	10% higher	Yes	Yes

aircraft measurements, airborne radar, and radiometer, and CRM simulations.

[13] NU-WRF was used for real time forecasts during the field campaign. It was initialized from the North American Mesoscale Model (NAM, 12 km spatial grid) from which time-varying lateral boundary conditions were provided at 3 h intervals. During the field campaign, two real-time NU-WRF forecasts (initialized at 00Z and 12Z, respectively, and integrated for up to 48 h) were conducted daily in support of aircraft operations. Ten precipitation events were selected for potential post-mission simulations (Table 2). These events include well-organized squall lines and scattered storms, which characterized the diurnal variation of rainfall in this area. The results from real-time forecast cases and one post mission case study are used for this study.

2.3. NLDAS Rainfall Data

[14] One-eighth-degree hourly assimilated rainfall datasets from the North American Land Data Assimilation System (NLDAS) [*Cosgrove et al*., 2003] Phase II is used to evaluate the NU-WRF simulations in this study. This rainfall dataset covers the conterminous U.S. and is most predominantly derived by temporally disaggregating CPC (Climate Prediction Center) PRISM (Parameter-elevation Regressions on Independent Slopes Model)-adjusted daily rain gauge data using hourly weights from NCEP Stage II Doppler radar precipitation estimates. Therefore, NLDAS rainfall data has a high temporal resolution, while retaining the magnitude of CPC daily rainfall data [*Higgins et al*., 2000]. Ten years of NLDAS rainfall data have been used to create a new benchmark of diurnal rainfall cycle climatology over the U.S. [*Matsui et al*., 2010].

[15] Table 3 shows the simulations performed for the post mission case study event. The North American Regional Reanalysis (NARR) was used to provide the initial as well as the boundary conditions at 3 h intervals. These sensitivity studies are designed to test the impact of surface fluxes, radiative processes, and terrain height on the precipitation processes for this MC3E case.

3. Results

3.1. Real Time Forecast Cases

[16] Hovmöller diagrams (Figure 3) are used to examine the model's ability to simulate the diurnal variation of precipitation (rainfall). Rainfall products from NLDAS and WRF simulations (for the 6 km horizontal resolution middle domain) are compared over the domain 34 to 37°N and 105 to 90°W. To remove uncertainties during model spin-up, only data from hours 4 to 28 from the WRF forecasts are used from each day for the comparison. The WRF predictions generally correspond to the precipitation events well, especially the heavy rainfall events (i.e., late April to early May and 20–25 May). The model, however, always tends to overestimate rainfall during light precipitation events (i.e., 9–19 May, late May to early June). It also over-predicts rainfall west of 100°. The model predications initialized at 12 UTC perform better as expected since 12 UTC is temporally closer to the typical convective initiation times (21–01 UTC) than the previous 00 UTC.

[17] Figure 4 shows time series of observed and model-predicted rainfall for 10 cases in Table 2. The model results capture the temporal variation for some of the cases as shown in NLDAS. For example, the 26 April, 1 May, and 20 May cases exhibit better temporal rainfall variation compared to other cases. These three cases, however, predicated peak intensities 2–3 h too early or too late compared to NLDAS. For other cases, the WRF-predicted rainfall is not in good agreement with NLDAS. The results also show that the predications initialized at a later time agree with the NLDAS-observed rainfall better in terms of intensity and peaks than the earlier initializations.

[18] Composites of the Hovmöller diagrams and domain-averaged rainfall are shown in Figures 5 and 6, respectively. Both figures show hourly precipitation averaged for the period 22 April to 3 June 2011. The model results show an afternoon onset (4 pm LST) of moist convection that agrees with the NLDAS rainfall. The WRF predictions also capture the nocturnal rainfall (from 7 P.M. to 3 A.M. LST) from the eastward-propagating MCSs on the lee side of the Rocky Mountains. In general, the WRF simulations capture the observed temporal variation of rainfall (Figure 6). Furthermore, the WRF results capture the observed diurnal precipitation peak (Figure 6). For example, the first rainfall maximum simulated by WRF is at 05 UTC, which agrees with observations [note that WRF is initialized at 00 UTC with a cold start (i.e., without clouds/precipitation, which requires a spin up time to produce rain)]. The magnitude of the first peak is also in good agreement with the observations. However, model performance deteriorates after 24 h of integration. For example, the model tends to underestimate the rainfall amount after 23 UTC. Nevertheless, the model-simulated rainfall peak from around 01 to 05 UTC is also in good agreement with observations. The other two diurnal modes (e.g., an afternoon rainfall maximum due to mesoscale and local circulations south and east of the Mississippi and Ohio valleys [*Carbone et al*., 2002; *Carbone and Tuttle*, 2008; *Matsui et al*., 2010]) are not simulated due to the model configuration and are not a focus of this study.

3.2. The 20 May Case Study

[19] One of the key physical components of NU-WRF is LIS. LIS is a high-resolution land data assimilation system that integrates the use of advanced land surface models, high-resolution satellite, and observational data, and data assimilation techniques. LIS features a high performance and flexible design, provides an interoperable infrastructure for hydrologic data assimilation and operates primarily on an ensemble of land surface models over user-specified regional or global domains. LIS has been coupled to the

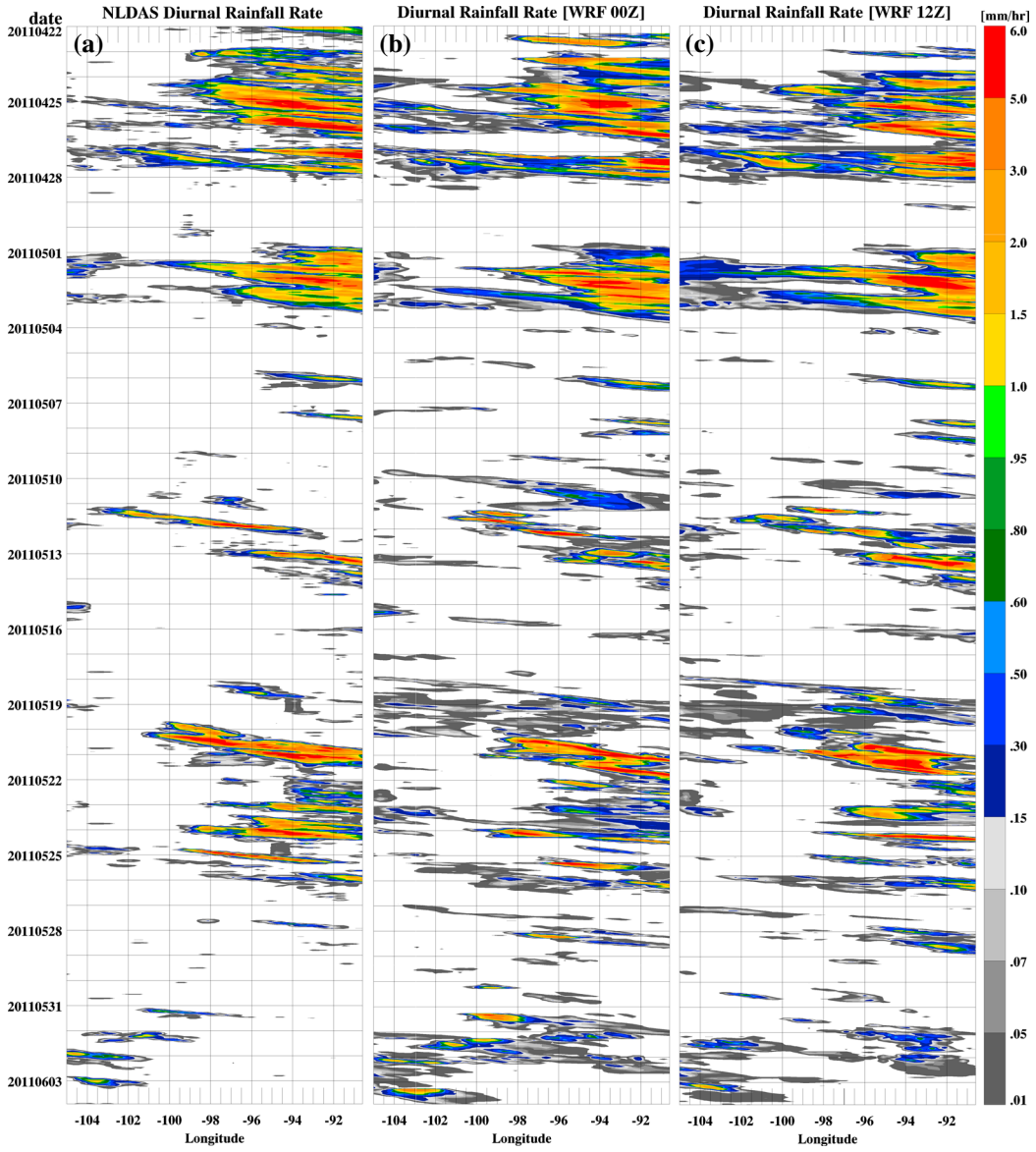

Figure 3. Hovmöller diagrams of hourly precipitation from (a) the North American Land Data Assimilation System (NLDAS) and WRF simulations initialized at (b) 00 UTC and (c) 12 UTC. The period is from 22 April to 3 June 2011. The local time is 5 h behind UTC. NLDAS has a resolution of 0.125°.

WRF ARW core [*Kumar et al*., 2007], enabling a coupled system to study land-atmosphere interactions. Land surface fields typically require long integration to reach thermodynamic equilibrium with the meteorology. The ability to conduct multiyear "spin-up" integrations therefore becomes important in generating accurate initial conditions consistent with the prescribed meteorological conditions. In the coupled mode, LIS directly interacts with WRF by acting as the land surface component and has the benefit of encapsulating several community land surface models, a broad set of data and a hydrological data assimilation infrastructure. Thus, the use of LIS enables the consistent use of the same physical schemes for both the generation of initial conditions and the coupled mode.

[20] On 20 May 2011, conditions were favorable for the development of a strong north-south oriented squall line in the general operations area of MC3E. A north-south oriented upper level trough situated over the Great Basin with jet-streak disturbances rotating around its base approached the central Oklahoma MC3E operations area on 19 May. Ahead of the trough, a dry line was located in the western Oklahoma panhandle, and east of the dry-line, a low-level, warm, moist Gulf return flow was situated over central to eastern Texas and Oklahoma. In association with these features, a broken line of supercell thunderstorms initially fired along the dry-line in the afternoon and evening of 19 May, and subsequently migrated slowly northward. As the eastward moving trough axis progressed further into New Mexico and Colorado during the early morning hours of 20 May, and embedded jet streaks rounded its base, the upper level environment coupled with the northward moving convection and a continuing south-southeasterly flow of warm-moist air ahead of the trough, enabled a large quasi-linear MCS with an associated deep line of

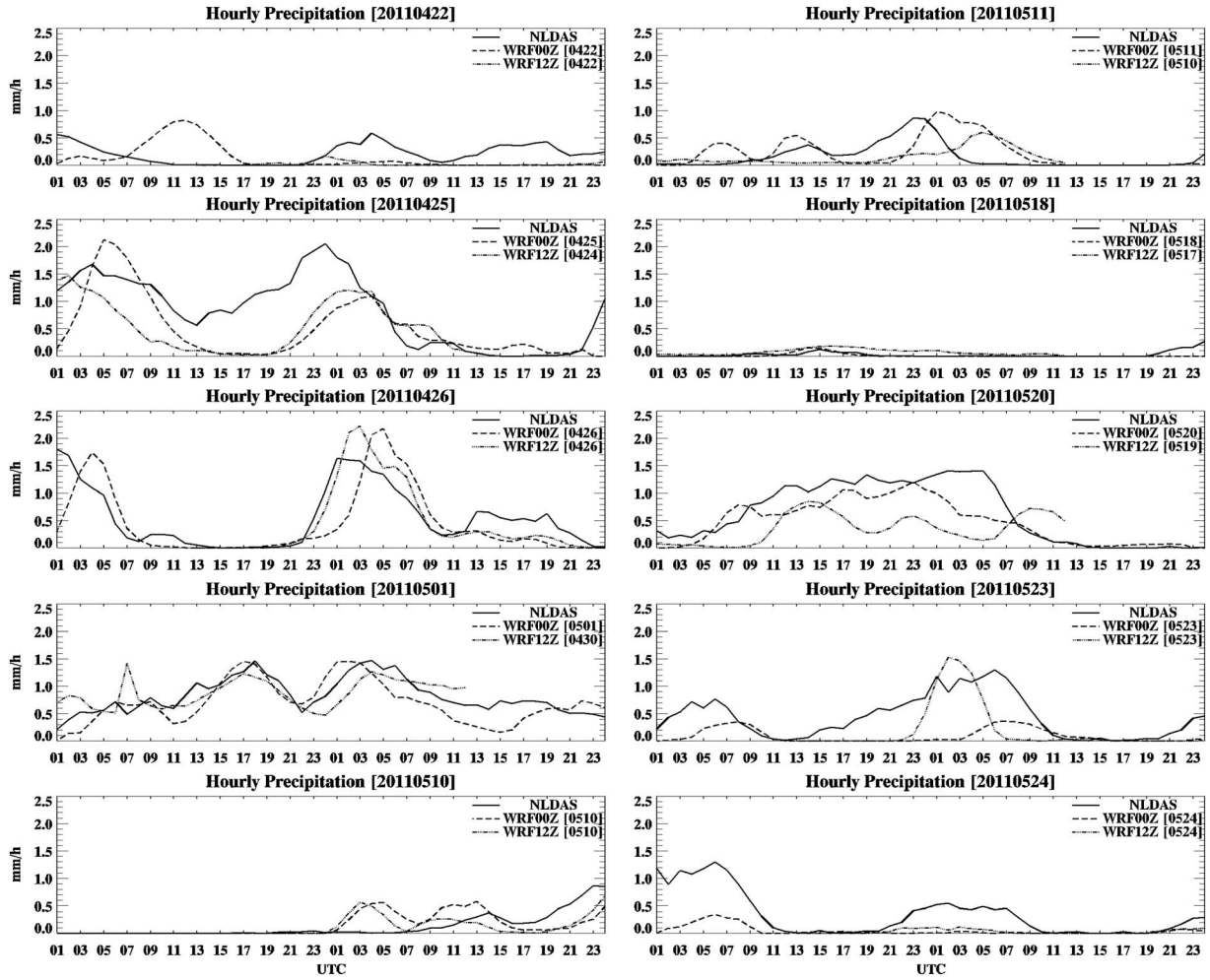

Figure 4. Time series of surface rainfall from all 10 cases shown in Table 2. Each panel shows the observed rainfall and results from two real-time WRF simulations initialized at 00 and 12 UTC. The precipitation is averaged over the domain 34 N to 37 N and 105 W to 90 W. The local time is 5 h behind UTC.

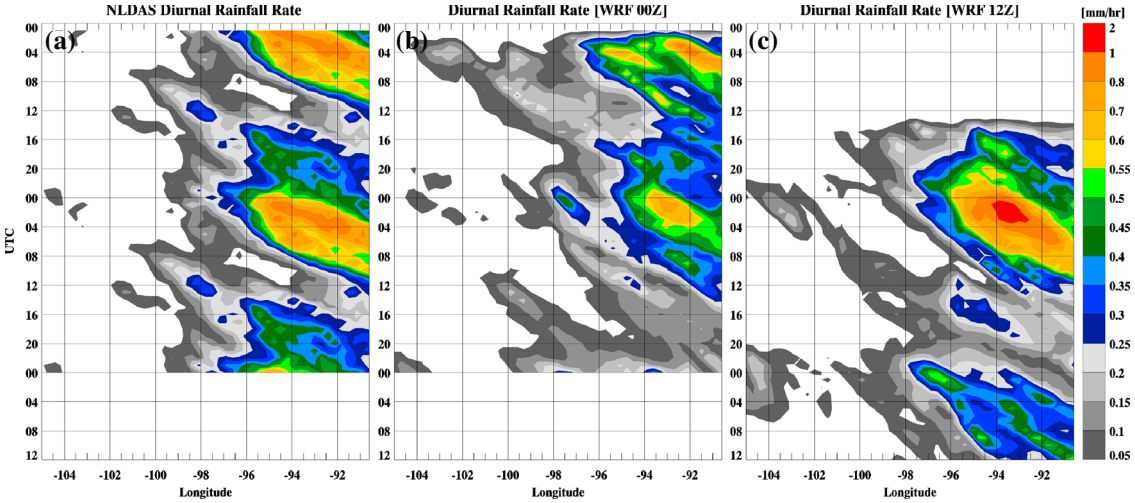

Figure 5. Hovmöller diagrams of hourly precipitation averaged over the period from 22 April to 3 June 2011. Data are from (a) the North American Land Data Assimilation System (NLDAS) and WRF simulations initialized at (b) 00 UTC and (c) 12 UTC. The NLDAS results are repeated after 24 h to be comparable with the WRF integration times (48 h). The local time is 5 h behind UTC.

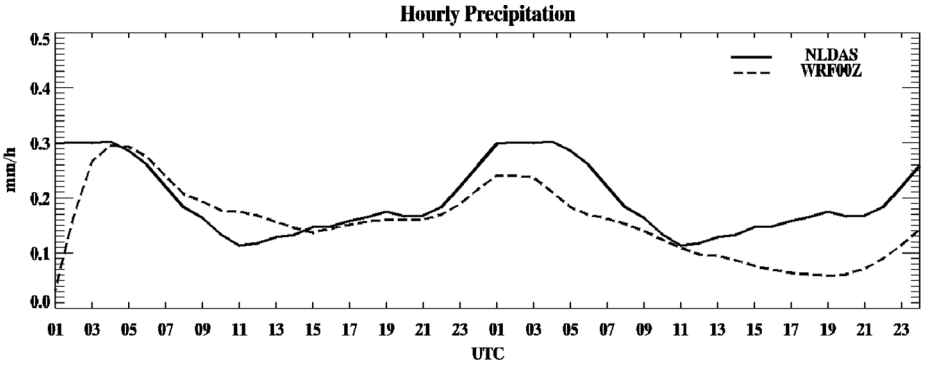

Figure 6. Time series of surface hourly precipitation averaged over the period 22 April to 3 June 2011 from NLDAS (solid line) and WRF initialized at 00 UTC (dashed line). The NLDAS results are repeated after 24 h to be comparable with the WRF integration time (48 h).

leading convection and broad region of trailing stratiform precipitation to develop and propagate across the MC3E observational domain.

[21] Two WRF simulations are conducted to study the impact of LIS on rainfall simulations on a diurnal scale. Both runs use NARR for the initial and lateral boundary conditions. The control run (named WLIS in Tables 3, 4, and 5) is coupled with LIS, and the soil temperature and moisture are from a LIS 6 year spin up where LIS was forced by NLDAS. The test run (named NOLIS) is not coupled with LIS, and its initial and boundary conditions (including soil temperature and moisture) come from NARR. Both runs use the Noah Land Surface Model. The soil moisture patterns are similar between NARR and LIS (Figure 7). NARR assimilates observed rainfall from the surface gauge network as well as hourly rainfall from NLDAS, which is the product of a temporal disaggregation of a gauge-only CPC analysis of daily precipitation performed directly on the NLDAS grid and includes an orographic adjustment based on the widely applied PRISM climatology. The LIS soil temperature and moisture distributions (which have the same resolution as WRF) also have more fine-scale structures than do the NARR (which are at 32 km resolution).

[22] Table 4 shows the domain mean latent and sensible heat fluxes from the runs with LIS and with NARR. The latent heat flux is 6.5 W/m^2 (9.5%) less on average in LIS compared to that from NARR despite the small differences in soil moisture at the initial time. On the other hand, the sensible heat flux is quite similar between LIS and NARR, even though LIS has a lower (colder) soil temperature (~3 K) on average than NARR initially. Soil type can affect sensible and latent heat flux; the domain average is less comparable between the two simulations. For example, higher soil moisture tends to increase latent heat flux while reducing sensible heat flux. If both latent and sensible heat fluxes are reduced, the available turbulent energy is reduced. This latter condition was found to arise from LIS having a slightly larger ground heat conductance than NARR (not shown).

[23] Figure 8a shows the simulated diurnal rainfall patterns for two runs with and without LIS (WLIS and NOLIS) for the 20 May case. Both runs captured the observed early and mature stages (09–23 UTC 20 May) as well as the decaying stage (09–15 UTC 21 May). The simulated rainfall is quite similar between the runs with and without LIS. The rainfall amount in the LIS run is slightly less than that in the NOLIS run, which had more surface available turbulent heat fluxes (the sum of the latent and sensible heat fluxes, Table 4). This indicates that the surface fluxes may affect the precipitation or that precipitation (and cloudiness) affects the surface fluxes. However, as the surface fluxes are not largely different between WLIS and NOLIS (Table 4), the degree to which they impact precipitation is hard to estimate. Thus, several additional runs have been conducted; their results are shown in section 4.

[24] For the 20 May case, the simulated rainfall (Figure 8a) captured the trend of the early, mature, and decaying stages. However, the total rainfall was underestimated by about 30%, and the time of peak rainfall, which was observed around 05 UTC 21 May, occurred too soon. Convective systems can be separated into convective and stratiform regions. There are several reasons for making this distinction [*Houze*, 1997]. Precipitation rates are generally much higher in the convective region. Ice particles tend to be rimed in the convective region and to be aggregates in the stratiform region. Microphysics and, as a consequence, rainfall and LH are also found to be different in these two regions (see the reviews by *Houze* [1997] and *Tao* [2003]). The convective and stratiform separation method developed for the GCE [*Tao and Simpson*, 1989; *Tao et al.*, 1993; *Lang et al*., 2003] was implemented into NU-WRF. The method is based on rainfall intensity (i.e., convective regions have higher rain rates) [*Churchill and Houze*, 1984], cloud updraft velocity (i.e., convective regions have stronger updrafts) [*Tao and Simpson*, 1989] and cloud species (i.e., convective regions have higher cloud water contents in the low to middle troposphere) [*Tao et al.*, 1993]. Please see *Lang et al.* [2003] for details on the convective-stratiform separation method including

Table 4. Domain Mean Soil Moisture and Temperature at Model Initialization, and Latent Heat Fluxes and Sensible Heat Fluxes From WRF Coupled with LIS and Without LIS Coupling[a]

	WLIS	NOLIS
Soil Moisture (%)	20	19
Soil Temperature (K)	297.49	300.07
Latent Heat (w/m^2)	61.3	67.8
Sensible Heat (w/m^2)	77.9	78.0

[a]Fluxes are Averaged Over 48 h of Model integration, upward is positive.

Table 5. Total Surface Rainfall (in mm) and its Convective and Stratiform Components From All Runs Including Real Time Forecasts[a]

Run	Total Rainfall (mm)	Convective (mm)	Stratiform (mm)
NLDAS	30.5		
WLIS	22.3	12.4	9.7
NOLIS	23.6	12.8	10.7
SFC1	20.7	10.4	10.3
SFC2	21.6	11.6	9.9
Rad1	19.9	10.6	9.0
TRAN1	19.4	11.9	7.4
TRAN2	19.2	11.1	7.9
TRAN3	22.9	12.1	10.7

[a]In addition, total rainfall from the North American land data assimilation system is also shown for comparison.

a comparison with other methods. The WRF results show that stratiform rain accounts for about 45% of the total rainfall amount (Table 5) and is about 12% to 15% more than has been observed in midlatitude squall lines based on rain gauge data [*Johnson and Hamilton*, 1988; *Johnson et al*., 1989]. However, this value does agree with *Houze* [1993] that the typical stratiform rain amount is about 25%–50% of the total rain when integrated over the lifetime of an MCS. The WRF simulations also do not show convective (stratiform) rain dominating in the early (decaying) stage (Figure 8b) as has been shown in previous observational [see *Houze*, 1993 Figure 9.12] and modeling studies [*Tao and Simpson*, 1989; *Tao et al*., 1991; and others].

[25] Figure 8c shows the temporal variation of liquid water path (LWP) and ice water path (IWP). The IWP is significantly more than the LWP and clearly indicates that ice processes are dominant for this continental MCS case. In addition, the IWP follows a diurnal variation similar to the surface rainfall variation. The importance of ice processes in organized convection with regard to the diurnal variation of surface rainfall was suggested by *Liu and Moncrieff* [1998]. The present results agree with *Liu and Moncrieff* [1998]. Figure 9 shows Hovmöller diagrams for the two runs WLIS and NOLIS; the results are quite similar. Furthermore, the simulated diurnal rainfall pattern is very similar to the climatology of nocturnal rainfall maxima due to eastward-propagating MCSs over the lee side of the Rockies [*Carbone et al*., 2002; *Carbone and Tuttle*, 2008; *Matsui et al*., 2010].

[26] Modeled and observed radar reflectivities are compared using a statistical technique developed by *Yuter and Houze* [1995], namely contoured frequency with altitude diagrams (CFADs). This technique computes the probability density of a field as a function of height. To achieve the most meaningful comparisons, the CFADs must be computed as similarly as possible between the model and radar-derived fields [*Lang et al*., 2007; *Matsui et al*., 2009], and an appropriate period from the model must be selected to compare with the observations. The resolution of the model data was also matched to that of the radar grid when possible. Gridded radar datasets were obtained from the National Mosaic and Multi-sensor QPE (NMQ), which

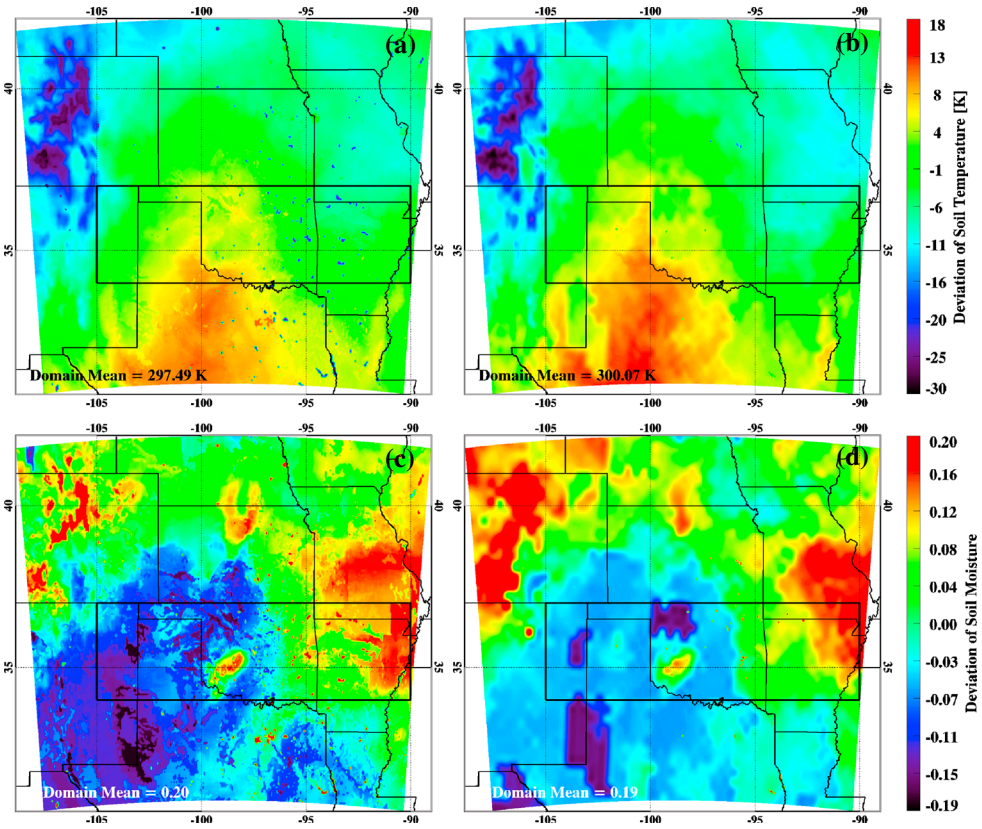

Figure 7. (top row) Soil temperature deviation in WRF at the initial time of 00 UTC 20 May 2011, (a) coupled with LIS and (b) without LIS. (c) and (d) are the same as Figures 7a and 7b except for soil moisture. Black boxes denote the domain for averaging.

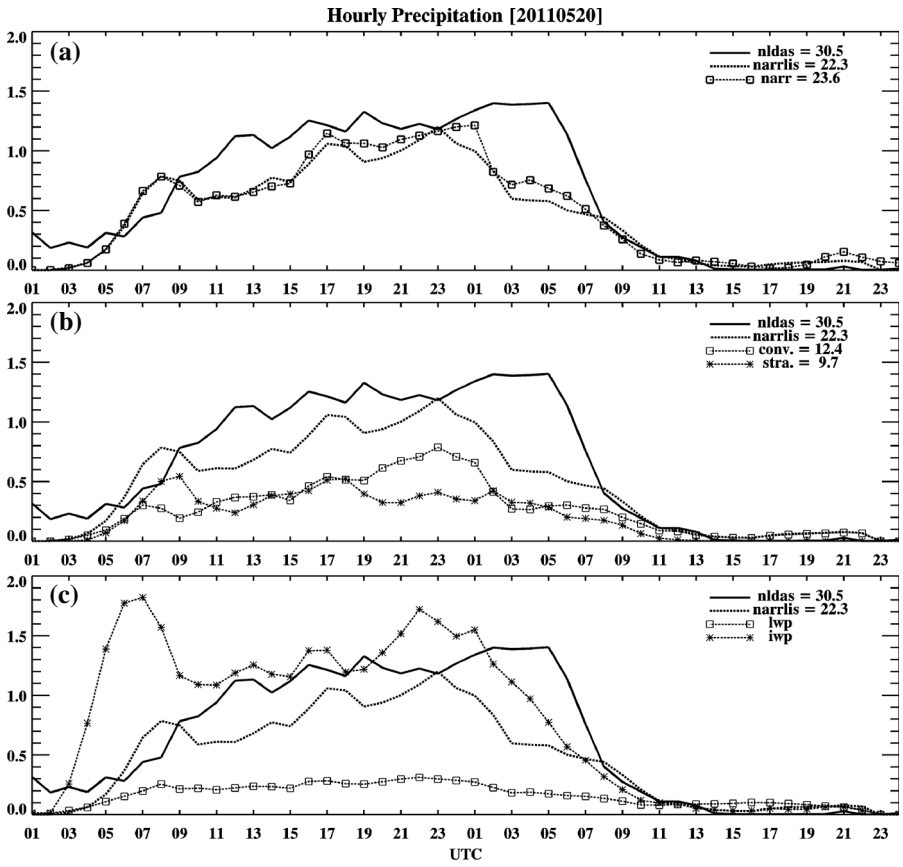

Figure 8. Time series of hourly precipitation from 00 UTC 20 May to 00 UTC 22 May 2011 from (a) NLDAS (solid), WRF coupled with LIS simulated precipitation (dashed), and WRF without LIS (dashed with squares). (b) NLDAS (solid) and WRF coupled with LIS for the total (dashed), convective (dashed with squares), and stratiform (dashed with asterisks) regions, and (c) NLDAS (solid), WRF coupled with LIS (dashed), and WRF-simulated liquid (dashed with squares) and ice water (dashed with asterisks) paths. Precipitation is in units of mm/h and liquid/ice water path in units of kg/m^2.

is based on Weather Surveillance Radar 88 Doppler (WSR-88D) radar observations nationwide [*Zhang et al.*, 2005]. The original data sets have a 5 min temporal and 1 km horizontal resolution. All of the Doppler analyses were performed on a 2 km horizontal grid. This matches the 2000 m grid used in the model, so no adjustment was made to the model data. Reflectivity CFADs were constructed by binning the reflectivities into 1 dBZ bins from 0 to 60 dBZ at each level. Figure 10a shows the observed CFADs. The highest probabilities follow a coherent pattern with the peak density steadily decreasing with height from between 20 and 35 dBZ near the melting level to between 5 and 15 dBZ near the storm top around 14–15 km. Maximum reflectivities are just over 55 dBZ between 4 and 7 km, around 55 dBZ at the surface, and drop off steadily aloft. However, below 4 km, there is a local maximum between 5–15 dBZ that is associated with active shallow stratiform clouds. The WRF-simulated CFAD (Figure 10b) has several notable differences with the observed (Figure 10a). For example, the modeled CFADs generally underestimate the peak reflectivity values (top 0.1%, shown in dark blue) at all levels below 0^{o}C. The differences are quite large at upper levels. In addition, just above the freezing level (between 4 and 6 km) the simulated frequency distribution peaks at both lower reflectivities (below 20 dBZ) and around 35 dBZ as opposed to the observed distribution, which peaks around 10 and 25 dBZ. If the simulated maxima at 35 dBZ were reduced, the results would be more comparable to the observations, since the frequency would shift to lower reflectivity values. However, the WRF-simulated CFADs capture the observed local maximum near 35 dBZ at lower levels.

[27] The simulated CFADs are also separated into the convective (Figure 10c) and stratiform regions (Figure 10d). At lower levels, the highest dBZ values (above 50 dBZ) occur mostly in the convective region. Below the freezing level, peak probabilities in the convective region are located around 40–45 dBZ and are around 30–40 dBZ in the stratiform region. Overall, the total CFAD inherits most of its features from the stratiform region, because the stratiform region covers a large part of the overall convective system in terms of area. The convective region, on the other hand, contributes to the higher reflectivity values due to the heavily rimed particles and large raindrops associated with the intense updrafts in that region.

[28] Figure 11 shows the horizontal distributions of hourly accumulated surface rainfall from NLDAS and WRF at four different times. The simulated rainfall intensity is stronger at the leading edge of the convective system (Figures 11g and 11h) than in the observations (Figures 11c

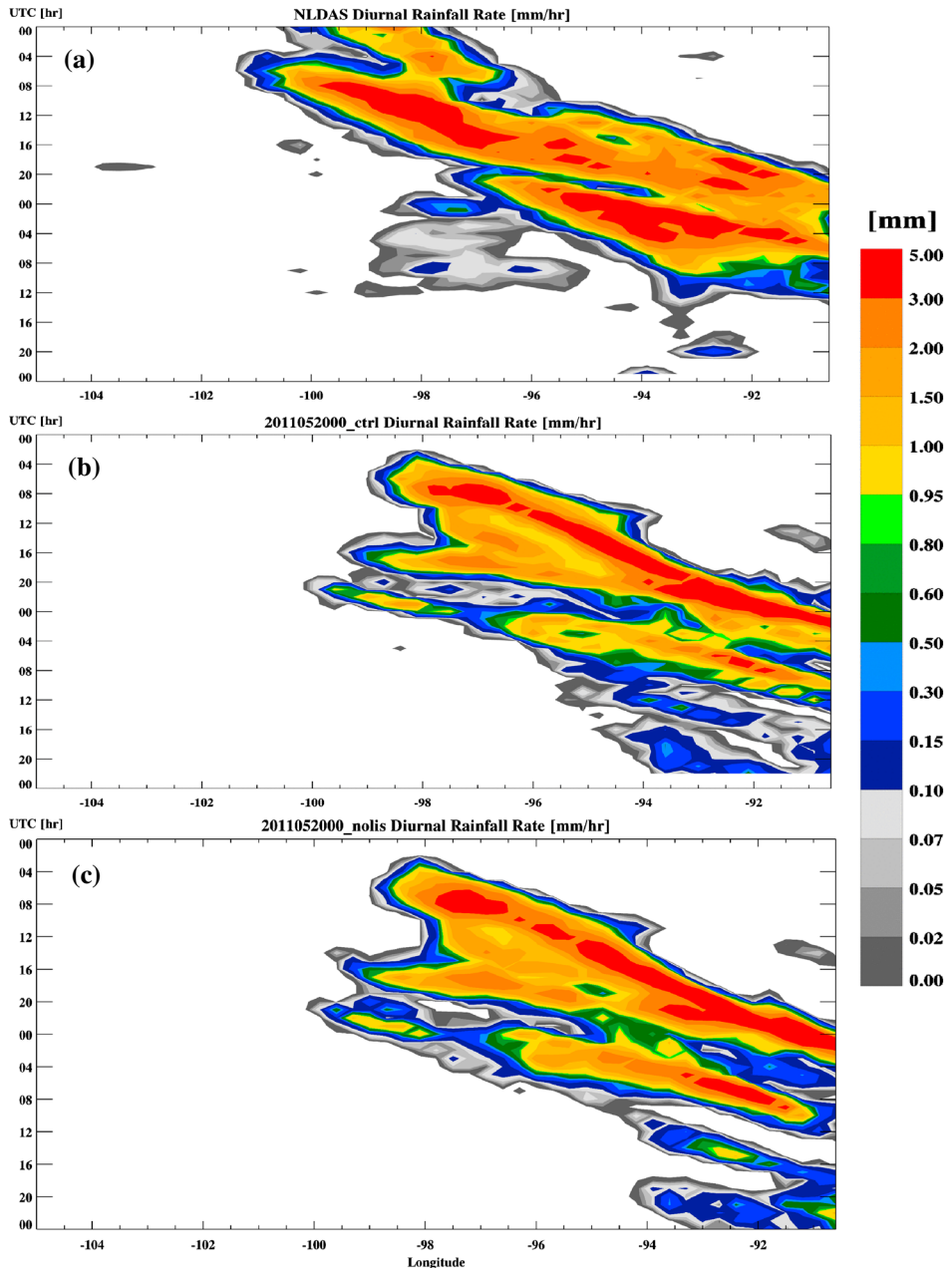

Figure 9. Hovmöller diagram of hourly precipitation from (a) NLDAS, (b) WRF coupled with LIS, and (c) WRF without LIS. The time period is from 00 UTC 20 May to 00 UTC 22 May 2011.

and 11d), while the simulated light precipitation area in the trailing stratiform region is too small when compared with the observations. Nevertheless, the simulated rainfall does capture some of the observed features. For example, precipitation starts with a linear structure (Figures 11a and 11e) and transitions to an arc shape later (Figures 11b–11d and 11h). Note that the resolution for NLDAS (0.125°) and the model (6 km grid spacing) are not the same. The lower resolution in NLDAS could reduce the rain intensities in the convective leading edge compared to the WRF simulations. Some of the model deficiencies might be caused by the model configuration as well as the physics (i.e., microphysics) used in the simulations.

[29] The observations show a classic continental multi-cell squall line structure ([*Rutledge et al.*, 1988; *Johnson and Hamilton*, 1988]; see a review by *Houze*, [1997]) with leading deep convective cells and a trailing stratiform region (Figure 12a). The model simulation also shows a deep convective cell at the leading edge followed by a wide stratiform region (Figure 12b); however, the simulated system lacks a uniform melting layer in the stratiform region for this case. There is a rear-to-front inflow that originates in the mid-troposphere and descends into the convective region (Figure 12c), and there are convective updrafts at the leading edge of the system above a pool of cold virtual potential temperature (Figure 12c). These features have been simulated by many previous modeling studies [i.e., *Rotunno et al.*, 1988; *Fovell and Ogura*, 1988; *Lafore and Moncrieff*, 1989; *Trier et al.*, 2006; *Moncrieff and Liu*, 2006; *Meng et al.*, 2012; and many others]. There are some notable differences between

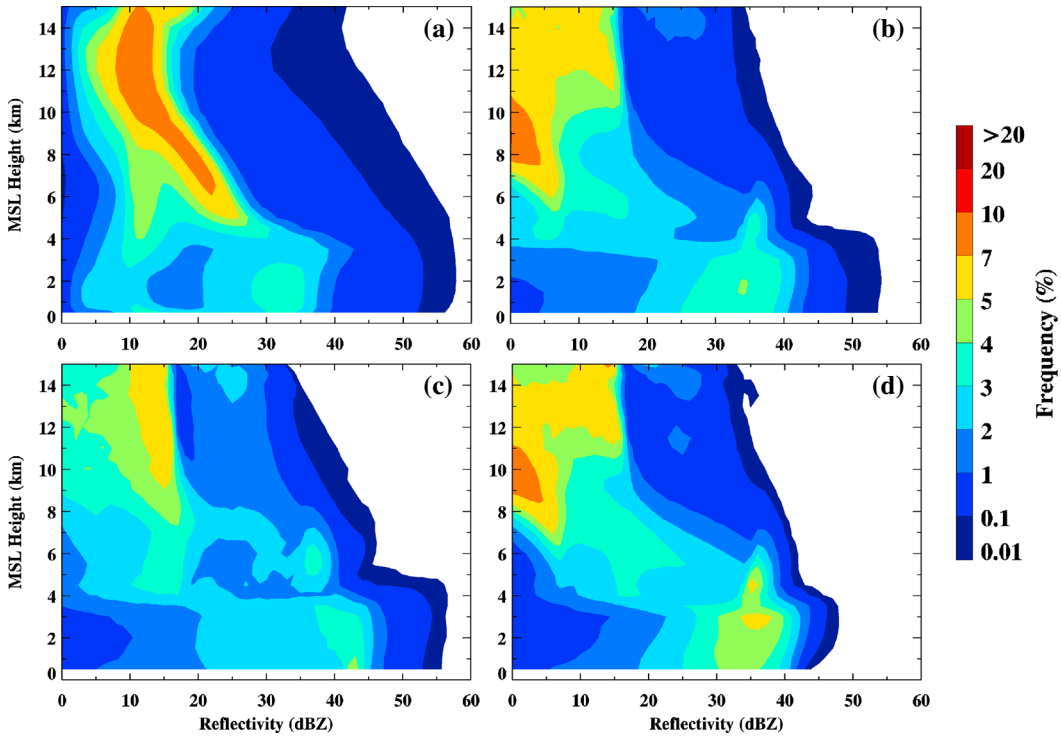

Figure 10. Radar reflectivity CFADs from (a) NEXRAD radar observations and WRF coupled with LIS for the (b) total, (c) convective, and (d) stratiform region. The CFADs are calculated from data every 10 min from 03 to 20 UTC 20 May. The dBZ bins range from 0 to 60 dBZ with a 1 dBZ bin interval.

the modeled and observed structures. For example, there is a distinct low-level convective cell prior to the main convective cell (Figure 12a) that is not simulated by the model. The observed stratiform region covers a much larger area (~200 km, Figure 12a) than does the simulated (~100 km, Figure 12b). These differences need to be investigated in future modeling research with a more detailed analysis of the microphysics via comparisons with MC3E aircraft and ground-based observations.

[30] Two additional runs were conducted to examine the impact of evaporative cooling on the diurnal variation of precipitation processes. In the first test, rain evaporation is turned off after 9 h of model integration in order to allow the initial development of convective systems. No convective systems develop if rain evaporation is turned off at the beginning of the model simulation. The simulated rainfall amount increases in this run compared to the control run (WLIS) and is in better agreement with observations both in terms of overall amount and the time of peak rainfall (Figure 13). Initially, the rainfall increases right after 09 UTC before starting to decrease at 10 UTC but is still greater than the WLIS control run until 20 UTC on 20 May. However, rainfall begins to increase again from 01 to 03 UTC on 21 May; this sudden dramatic increase in rainfall does not agree with the observations. Overall, the simulation overestimates the rainfall amount after 07 UTC May 21. There are two opposing effects on surface rainfall by not allowing rain evaporation. The first one is the dynamic effect: the strength of the downdrafts as well as the low-level cool pool is reduced. Reducing the cold pool and downdrafts, which both serve to generate new cells and maintain squall line development and structure, can lead to less overall precipitation. The second effect is a microphysical effect: if rain does not evaporate, more can reach the surface, which would increase the overall rain amount. The second effect could explain the enhanced rainfall. However, the cloud water amount in the lower troposphere was reduced due to the relatively dry environment (there would be less water vapor without rain evaporation). Therefore, a second additional run was conducted wherein both rain and cloud evaporations were turned off. The total rainfall in this run is actually less (Figure 13), because the propagating MCS begins to decay after 19 UTC 20 May compared with the control run (WLIS).

[31] The interaction between LH and environmental shear is fundamental to the dynamics of MCS-type convective organization. The effect of cold pool and gust front dynamics on long-lasting squall lines has been studied extensively using numerical models [e.g., *Rotunno et al.*, 1988; *Fovell and Ogura*, 1988; *Weisman et al.*, 1988; *Tripoli and Cotton*, 1989a, 1989b; and many others] and observations [e.g., *Wakimoto*, 1982]. Figure 14 shows the virtual potential temperature perturbation (θ_v') and surface rainfall for the control run (WLIS) and the runs without rain evaporative cooling and without rain or cloud evaporation. The environmental virtual potential temperature ($\overline{\theta_v}$) is computed by averaging the virtual potential temperature over the domain 34°N to 37°N and 105°W to 90°W. The virtual potential temperature perturbation ($\overline{\theta_v}$) is the actual virtual potential temperature ($\overline{\theta}_a$) minus the environmental virtual potential temperature ($\overline{\theta_v}$), whereas ($\overline{\theta}_a$) is the actual virtual potential temperature over a rectangular area (0.3×0.3 degrees centered on the gust front). For the WLIS

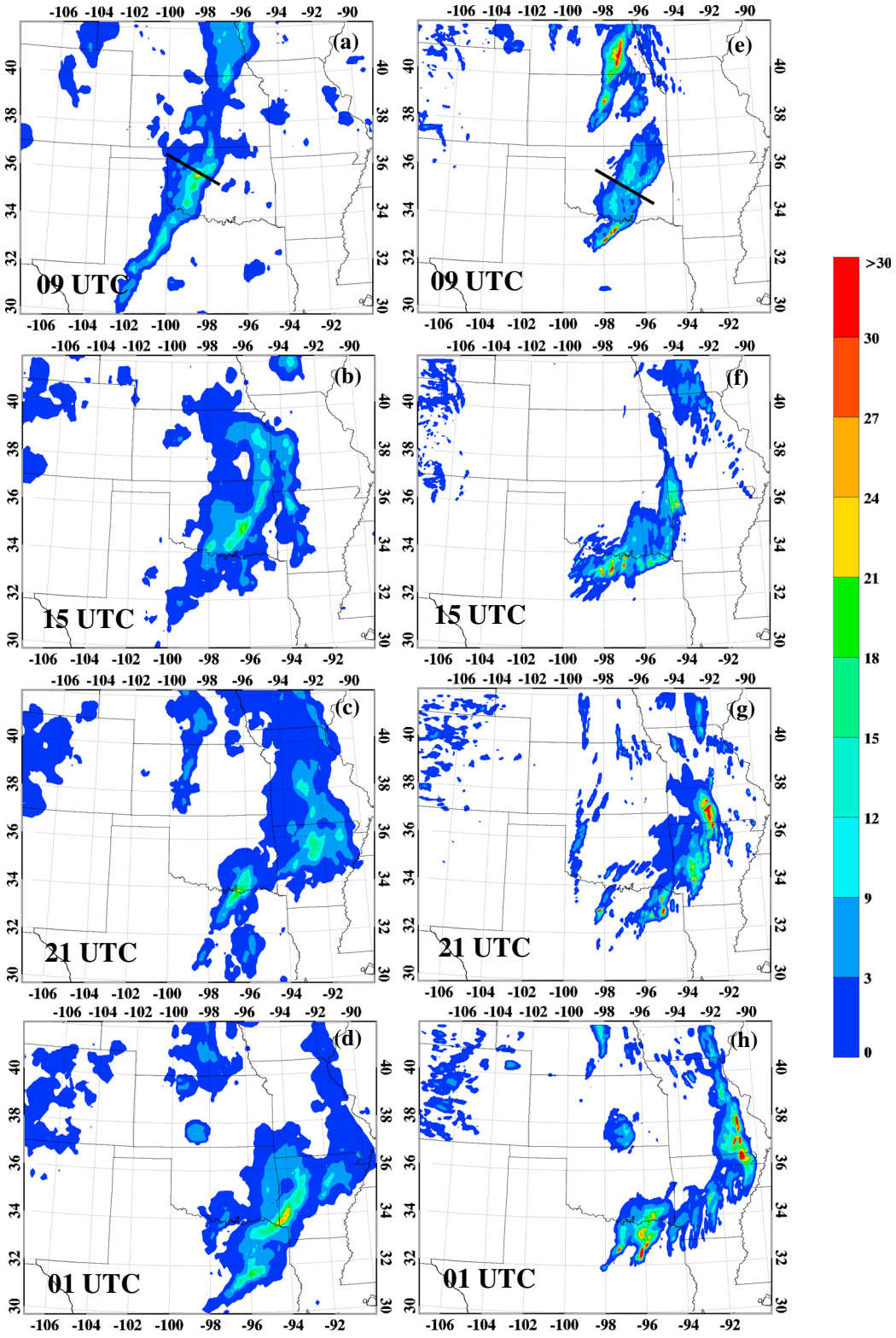

Figure 11. Hourly accumulated surface rainfall (in mm) from (a)–(d) NLDAS, and (e)–(h) the WRF simulation with LIS. Figures 11a and 11e are at 09 UTC, 11b and 11f at 15 UTC, 11c and 11g at 21 UTC 20 May, and 11d and 11h are at 01 UTC 21 May 2011.

control run, the rainfall is ahead of the cold θ_v' for the convective event that developed during the first 9 h of model integration. Thereafter, the surface cold pool (cold θ_v') and rainfall are collocated for the major rainfall event that developed after 11 UTC (see Figures 9b and 11). This rainfall (and its associated convective system) is propagating eastward along with the pool of cold θ_v'. The cool pool is much weaker in the runs without rain or without cloud and rain

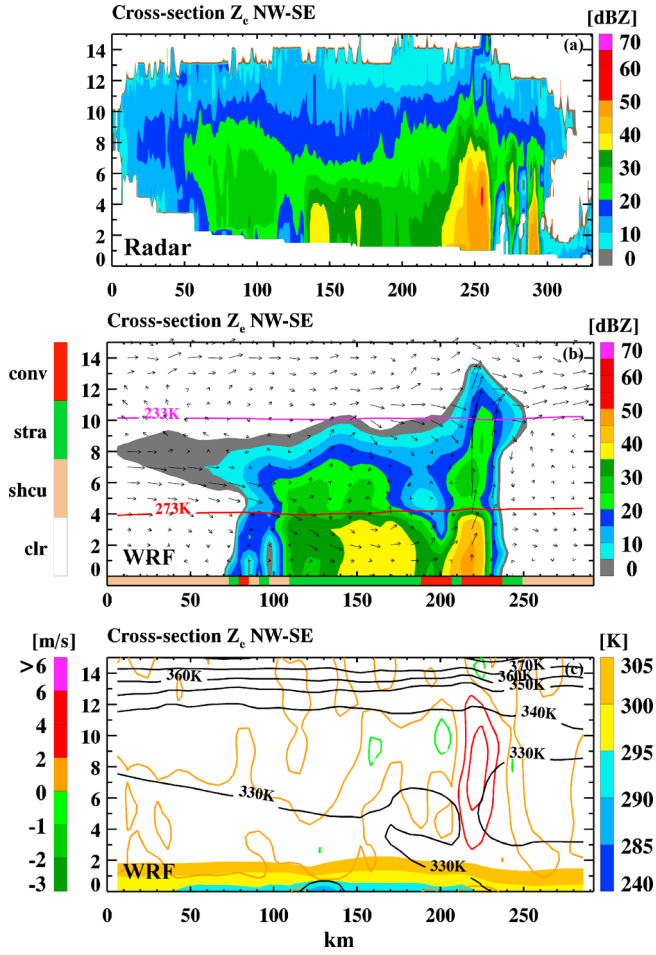

Figure 12. Vertical cross-sections of (a) radar reflectivity from NEXRAD, (b) reflectivity and winds from WRF with LIS (convective-stratiform partitioning is marked below the reflectivity field), and (c) vertical velocity (colored contours), equivalent potential temperature (black contours), and virtual potential temperature deviation (filled contours) from WRF with LIS at 09 UTC on 20 May 2011. Positions of cross-section lines are shown in Figures 11a and 11e for radar observations and WRF simulations, respectively.

evaporation than in the control run (WLIS). The simulated eastern-most convective systems in those runs have a shorter lifetime. These additional sensitivity tests suggest the cold pool plays an important role in the propagating convective system associated with diurnal rainfall for this case. These additional simulations also suggest that the evaporation of liquid water can have a major impact on precipitation processes. Therefore, knowledge (i.e., observations) of the size distribution of liquid water is needed to better estimate evaporative processes.

[32] It is interesting to note that the convection that developed near and after 00 UTC 21 May is stronger in the two runs without evaporation (Figures 13 and 14). This is also in better agreement with the NLDAS observations than the control run (WLIS) and is due to the rapid intensification of convective cells from shallow cumulus. These convective cells are located to the west of the main convective system (not shown). Rain evaporation may have a different impact on organized squall lines and less-organized convective cells due to their apparent dynamical structures. However, runs with no evaporation could not sustain the first propagating convective cells. There may be other physical processes involved and requires future study.

4. Sensitivity Tests

4.1. Surface Fluxes

[33] Sensible and latent heat fluxes over land have strong diurnal variation. In addition, land surface (continental thermal) forcing plays a major role in the thermodynamic instability within the PBL [*Pielke*, 2001]. Two sensitivity tests were conducted in which the surface turbulent fluxes were reduced by 100% (i.e., no surface fluxes, SFC1) and by 50% (SFC2), respectively. The results show that rainfall is slightly reduced: by 10% in the SFC1 run and 5% in the SFC2 run (Table 5). The temporal variation of rainfall is similar between the control (WLIS) and two sensitivity runs except that the SFC1 and SFC2 runs have smaller rainfall after 18 UTC (Figure 15). The peak rainfall amount is actually quite similar in these three runs. These results suggest that reducing the surface fluxes does not significantly alter the peak in the diurnal rainfall pattern even when they are significantly different. The 20 May case is a propagating MCS-type event that was initiated over the Rocky Mountains. Once convective systems become organized and start to propagate, variations in surface turbulent fluxes do not significantly affect their propagation and organization.

[34] CRMs have examined the mechanism associated with the diurnal variation of precipitation processes in the Tropics [*Tao et al.*, 1996; *Sui et al.*, 1998]; (see reviews by *Tao* [2003] and *Tao and Moncrieff* [2009]). *Sui et al.*

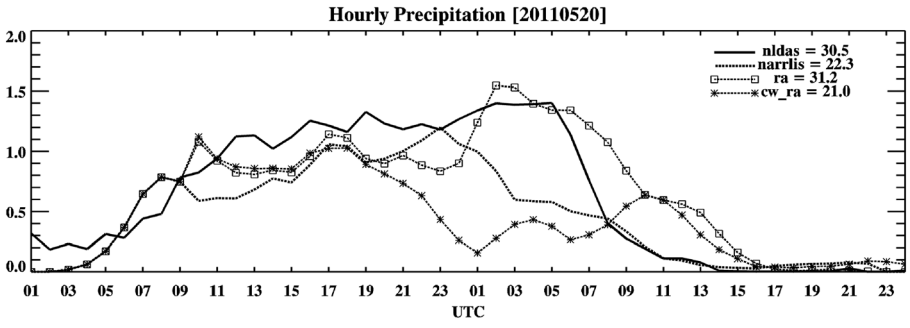

Figure 13. Same as Figure 8a except for the run without rain evaporative cooling (dashed with squares) and the run without rain or cloud evaporative cooling (dashed with asterisks).

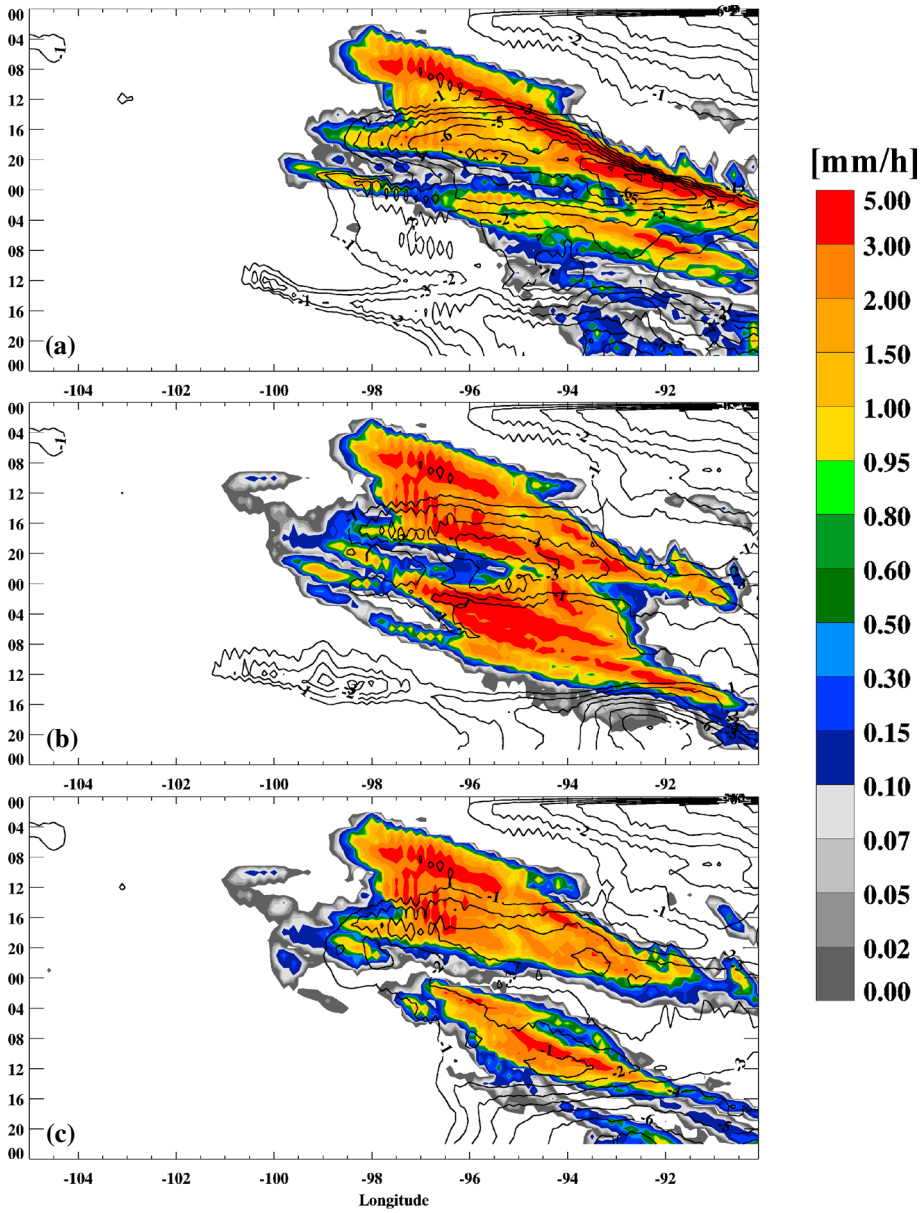

Figure 14. Hovmöller diagram of hourly precipitation (filled contours) and surface virtual potential temperature perturbation (VPT at the lowest model level minus the domain-averaged VPT at each hour, overlaid in black) from the (a) WRF simulation with LIS, (b) WRF simulation with LIS but without rain evaporation, and (c) WRF simulation with LIS but without cloud or rain evaporation at 09 UTC on 20 May. The entire period is from 00 UTC 20 May to 00 UTC 22 May.

[1998] conducted sensitivity tests to examine the impact of the diurnal variation of SST (sea surface temperature) and found that the diurnal variation of rainfall was well simulated even when the diurnal variation of SST was suppressed. They concluded that while the diurnal variation of sea surface temperature modulates rainfall processes, it might play a secondary role in the diurnal variability. The results presented here are consistent with *Sui et al*. [1998] in that surface fluxes do not have a primary role in the diurnal variation of rainfall with regard to organized propagating convective systems.

[35] *Trier et al*. [2011] also conducted sensitivity tests that indicated that surface heating has little effect on the strength and structural characteristics of an MCS. However, surface heating became the primary forcing for the MCS during the midday (6–7 h after model integration). Our results partially agree with *Trier et al*. [2011] that surface heating has little effect on the strength and structural characteristics of an MCS.

4.2. Radiation

[36] The interaction between clouds and radiation is two-way. On one hand, clouds can reflect incoming solar and outgoing longwave radiation. On the other hand, radiative heating/cooling can enhance or reduce cloud activity including precipitation and its diurnal variation in the Tropics (see *Tao et al*. [1996], *Sui et al*. [1998], and a review by *Tao*, [2003]). For example, a high-resolution

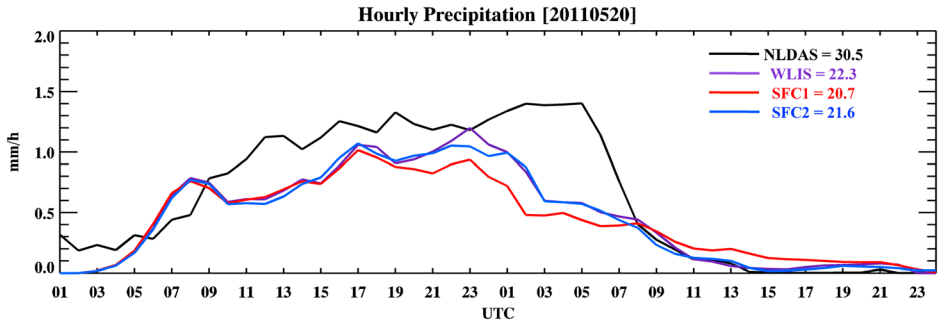

Figure 15. Time series of hourly precipitation from 00 UTC 20 May to 00 UTC 22 May 2011 from (a) NLDAS (black), WRF coupled with LIS simulated precipitation (WLIS, shown in purple), the runs with sensible and latent heat fluxes turned off throughout the simulation (SFC1, shown in red) and reduced by 50% throughout the simulation (SFC2, shown in blue).

cloud-resolving simulation that did not allow for the diurnal variation of radiative processes failed to produce a diurnal variation of rainfall. *Sui et al*. [1998] found that modulation of convection by the diurnal change in available water (or relative humidity), which is a function of temperature, was responsible for a maximum rainfall after midnight. This implies that the increase (decrease) in surface precipitation associated with longwave cooling (solar heating) was due to an increase (decrease) in relative humidity [*Tao et al*., 1996]. Other physical processes (convective organization and its associated ice processes and atmospheric stability) have been proposed by *Liu and Moncrieff* [1998] and *Xu and Randall* [1995] as having a role in the diurnal variation of precipitation based on CRM simulations. In addition, *Tao et al*. [1996] found that radiation has a bigger impact on tropical oceanic convection than its midlatitude continental counterpart.

[37] One sensitivity test is conducted to examine the impact of radiation on precipitation processes and their associated diurnal variation. In run Rad1, solar heating and long-wave cooling are tuned off; this reduced the simulated rainfall amount by about 10% (Table 5). For a PRE-STORM squall line simulation, *Tao et al*. [1996] found that precipitation was reduced by 8% for a run without long-wave cooling. In contrast, long-wave cooling led to a 36% increase in rainfall for a tropical case. They suggested that the higher CAPE and lower humidity environment in PRE-STORM could be the reason for the reduced impact of radiation on precipitation. The present modeling results are consistent with *Tao et al*. [1996].

[38] Simulated rainfall was slightly reduced from 07 to 11 UTC (2 to 6 A.M. LST) on 20 May and 21 UTC 20 May to 03 UTC 21 May (4 to 10 P.M. LST 20 May, Figure 16). On the other hand, rainfall increased from 11 to 20 UTC (6 A.M. to 3 P.M. LST) on 20 May. The results show that without long-wave cooling, rainfall is reduced (increased) during the late afternoon and on into midnight and during the early morning (during the early morning to early afternoon). The enhancement of rainfall by long-wave cooling in the early morning is in very good agreement with previous CRM simulations for tropical events [*Tao et al*., 1996; *Sui et al*., 1998]. The reduction in rainfall by solar heating is also in good agreement with previous CRM simulations [*Tao et al*., 1996].

4.3. Terrain

[39] Terrain has a primary effect on the initiation of convective systems and the nocturnal rainfall maxima associated with eastward-propagating MCSs on the lee side of the Rocky Mountains [*Carbone et al*., 2002; *Carbone and Tuttle*, 2008; *Matsui et al*., 2010]. Three sensitivity tests were conducted on the terrain effect: no terrain (run TRAN1), terrain decreased by 50% (run TRAN2) and terrain heights increased by 10% (run TRAN3). The reason for performing run TRAN3 is that the 2 km grid resolution in the model could underestimate the actual terrain height, because WRF terrain is smoothed more than the grid spacing for stability.

[40] The results show that increasing the terrain height by 10% (run TRAN3) increases the simulated rainfall amount, which is in slightly better agreement with observations

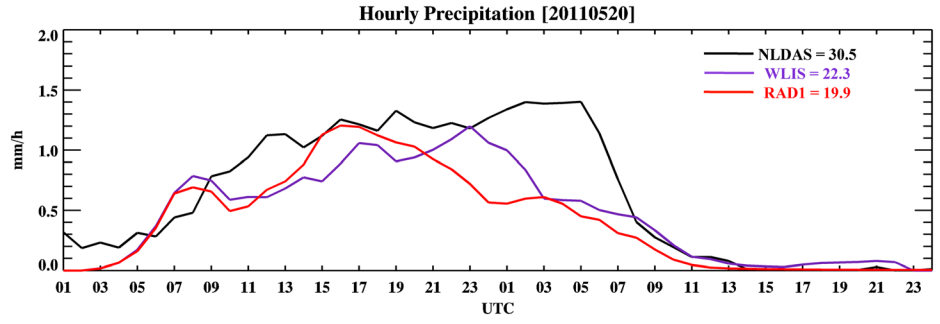

Figure 16. Same as Figure 15 except for the run with radiation processes completely turned off (RAD1, shown in red).

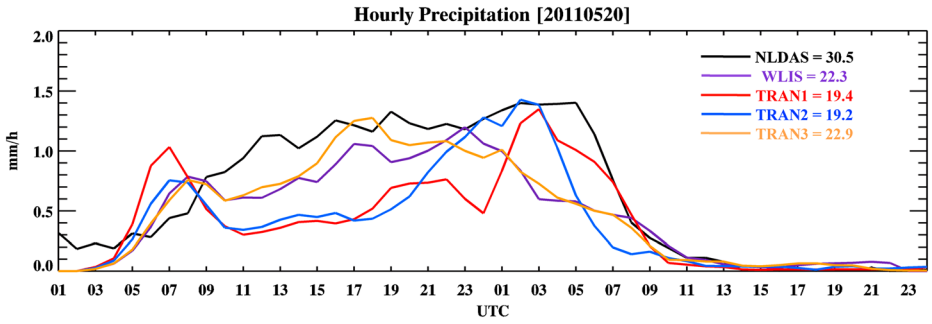

Figure 17. Same as Figure 16 except for the run without terrain (TRAN1, shown in red), terrain reduced by 50% (TRAN2, shown in blue), and terrain enhanced by 10% (TRAN3, shown in gold).

(Table 5). The temporal variation of simulated rainfall in run TRAN3 is stronger than the control run (WLIS) on the first day of model integration and also in better agreement with observations (Figure 17).

[41] The simulated rainfall is reduced about 13–14% for runs TRAN1 and TRAN2 compared to the control run (WLIS). Decreasing the terrain height by 50% (TRAN2) and 100% (TRAN1) results in much less rainfall during the initial and major development period (11–24 UTC) and is in poorer agreement with observations. These modeling results confirm the previous observational studies that terrain plays a primary role in the diurnal variation of rainfall (especially in the initial developing stage) for these types of cases.

5. Summary

[42] In this study, NU-WRF was used to conduct a series of simulations of summer time convective events east of the Rockies that occurred during MC3E; the simulation results were then used to evaluate the model's ability to capture the diurnal rainfall cycle. The model physical packages included an improved microphysics scheme that reduces unrealistically high 40 dBZ echoes aloft [*Lang et al*., 2011] and a sophisticated land surface modeling system (i.e., LIS) [*Kumar et al*., 2006]. This version of NU-WRF was used at high-resolution (2 km horizontal grid spacing for the innermost domain) to simulate observed rainfall events and to conduct sensitivity tests to examine the impact of surface fluxes, radiation, and terrain on the diurnal variation of surface rainfall. The major highlights are as follows:

[43] 1. NU-WRF has the ability to predict heavy precipitation events as well as the collective diurnal variation of rainfall for the cases during MC3E. However, for individual cases, only three out of 10 simulations showed a high degree of accuracy in predicting precipitation, due to location errors and misrepresentation of convective intensity. In addition, the model tends to overestimate rainfall during light precipitation events.

[44] 2. The model can capture the rainfall trend during the early, mature, and decaying stages of the 20 May 2011 MCS case. However, the total rainfall is underestimated, and the time of peak rainfall is earlier than was observed.

[45] 3. The temporal variation of simulated rainfall is quite similar between runs using two different sets of initial soil temperature and moisture conditions. Both runs produce multi-cellular-eastward propagating MCSs as observed.

[46] 4. The model-simulated radar reflectivity probabilities (i.e., CFAD) have a local maximum at 35 dBZ in the lower troposphere that is in good agreement with observations. This low-level maximum is mainly due to precipitation from the extended stratiform region. The convective region, on the other hand, contributes to the higher (50 dBZ) reflectivity values.

[47] 5. The model results indicate that the cold pool and rainfall are closely related, which suggests that cold pool dynamics are the predominant physical process for the maintenance and propagation of the multi-cellular 20 May MCS, which is in good agreement with previous modeling studies. Turning off the evaporative cooling of rain or the evaporative cooling of cloud and rain leads to a weaker cold pool and as a result a shorter MCS life cycle. However, these sensitivity tests also show some non-linear effects on the propagation of secondary convection.

[48] 6. The model results indicate that surface heat and moisture fluxes, which were obtained from a land information system (including the spin up of the initial soil temperature and moisture conditions), play only a minor role in terms of the phasing of diurnal variation for the 20 May propagating MCS case. Surface fluxes only affect the rainfall amount slightly (less than 10%). This result is also consistent with previous modeling results.

[49] 7. The model results indicate that the terrain effect is important for the initial stages of MCS development. The amount of simulated rainfall increases and is in better agreement with observations when the terrain height is increased by 10%.

[50] 8. The model results indicate that radiation does not play a major role in the simulated diurnal variation of rainfall. Simulated rainfall for the 20 May case is reduced by 10% when solar heating and long-wave cooling are turned off. The model results indicate that solar heating (long wave cooling) can reduce (enhance) the amount of rainfall, which also agrees with previous modeling results.

[51] The above results are only based on one propagating MCS case. Additional MC3E case studies are needed. Specifically, two cases, 25–26 April and 1 May for which NU-WRF simulated the diurnal variation of rainfall well (see Figure 4), will be studied. These two MC3E cases and the 20 May case are among the priority cases for observational study for addressing microphysical processes (i.e., drop size distributions). In these post-mission model simulations, a larger inner domain and finer grid spacing (1 km or finer) will be needed. Finally, further sensitivity tests with the

other bulk microphysical schemes [i.e., *Morrison et al*., 2005 and a recently developed Goddard 4ICE scheme] as well as spectral bin microphysics [i.e., *Iguchi et al*., 2012] are needed.

[52] The conclusions from this study also infer why global climate/weather models can have a difficult time capturing the diurnal variation of rainfall over the Great Plains [*Lee et al*., 2007]. Typically, the grid spacing in global models is a few hundred kilometers and, as a result, these models: (1) cannot properly resolve terrain and therefore terrain-induced convection, (2) rely upon a mass-flux-based convective parameterization that cannot explicitly induce/resolve cold-pool dynamics and gravity wave structures, and thus, (3) have a difficult time reproducing propagating convective rainfall systems on the lee side of mountains. Subgrid parameterization of these processes is a great challenge in the community; the obvious brute-force solution is to run global models at cloud-resolving or cloud-permitting resolution (i.e., a horizontal grid spacing of a few kilometers). A few global models have achieved such resolutions [*Satoh et al*., 2008; *Putman and Suarez*, 2011], and obviously, these cloud-resolving global models will play a critical role in simulating rainfall variability in the future.

[53] **Acknowledgments.** The authors appreciate the hard work and effort of all those who planned and participated in the MC3E field campaign. We thank R. Johnson and S. Rutledge at Colorado State University for discussions on stratiform rain amounts. We would also like to thank Anil Kumar at Goddard for providing the LIS spin-up data sets. Carrie Langston at the National Severe Storm Laboratory provided invaluable help in the NEXRAD NMQ data product. The authors acknowledge the NASA Ames Research Center and the NASA Goddard Space Flight Center for the computer time used in this research. We also thank three anonymous reviewers for their constructive comments that improved this paper significantly. This research was supported by NASA Precipitation Measurement Mission (PMM), NASA Modeling Analysis Prediction (MAP), and the Office of Science (BER), U. S. Department of Energy/Atmospheric System Research (DOE/ASR) Interagency Agreement DE-AI02-04ER63755. MC3E is a NASA-DOE joint field campaign.

References

Carbone, R. E., and J. D. Tuttle (2008), Rainfall occurrence in the U.S. warm season: The diurnal cycle, *J. Clim.*, *21*, 4132–4146.

Carbone, R. E., J. D. Tuttle, D. A. Ahijevych, and S. B. Trier (2002), Inferences of predictability associated with warm season precipitation episodes, *J. Atmos. Sci.*, *59*, 2033–2056.

Chin, M., R. B. Rood, S.-J. Lin, J. F. Muller, and A. M. Thomspon (2000), Atmospheric sulfur cycle in the global model GOCART: Model description and global properties, *J. Geophys. Res.*, *105*, 24,671–24,687.

Chin, M., P. Ginoux, S. Kinne, B. N. Holben, B. N. Duncan, R. V. Martin, J. A. Logan, A. Higurashi, and T. Nakajima (2002), Tropospheric aerosol optical thickness from the GOCART model and comparisons with satellite and Sun photometer measurements, *J. Atmos. Sci.*, *59*, 461–483.

Chin, M., D. A. Chu, R. Levy, L. Remer, Y. Kaufman, B. Holben, T. Eck, P. Ginoux, and Q. Gao (2004), Aerosol distribution in the Northern Hemisphere during ACE-Asia: Results from global model, satellite observations, and Sun photometer measurements, *J. Geophys. Res.*, *109*, D23S90, doi:10.1029/2004GL02014.

Chou, M.-D., and M. J. Suarez (1999), A solar radiation parameterization for atmospheric studies, *NASA Tech. Rep.*, *15*, 38, NASA/TM-1999-10460.

Chou, M.-D., and M. J. Suarez (2001), A thermal infrared radiation parameterization for atmospheric studies, *NASA Tech. Rep.*, *19*, 55, NASA/TM-2001-104606.

Churchill, D. D., and R. A. Houze, Jr. (1984), Development and structure of winter monsoon cloud clusters on 10 December 1978, *J. Atmos. Sci.*, *41*, 933–960.

Clark, A. J., W. A. Gallus, and T. C. Chen (2007), Comparison of the diurnal precipitation cycle in convection-resolving and non-convection-resolving mesoscale models, *Mon. Wea. Rev.*, *135*, 3456–3473.

Cosgrove, B. A., D. Lohmann, K. E. Mitchell, P. R. Houser, E. F. Wood, J. C. Schaake, A. Robock, C. Marshall, J. Sheffield, and Q. Duan (2003), Real-time and retrospective forcing in the North American Land Data Assimilation System (NLDAS) project, *J. Geophys. Res.*, *108*(D22), 8842, doi:10.1029/2002JD003118.

Dai, A. G., F. Giorgi, and K. E. Trenberth (1999), Observed and model-simulated diurnal cycles of precipitation over the contiguous United States, *J. Geophys. Res.*, *104*, 6377–6402.

Davis, C. A., K. W. Manning, R. E. Carbone, S. B. Trier, and J. D. Tuttle (2003), Coherence of warm-season continental rainfall in numerical weather prediction models, *Mon. Wea. Rev.*, *131*, 2667–2679.

Fovell, R. G., and Y. Ogura (1988), Numerical simulation of a midlatitude squall line in two-dimensions, *J. Atmos. Sci.*, *45*, 3846–3879.

Grell, G. A., and D. Devenyi (2002), A generalized approach to parameterizing convection combining ensemble and data assimilation techniques, *Geophy. Res. Lett.*, *29*(14), 1693, doi:10.1029/2002GL015311.

Higgins, R. W., W. Shi, E. Yarosh, and R. Joyce (2000), Improved United States precipitation quality control system and analysis, NCEP/Climate Prediction Center ATLAS, *7*, 40.

Hong, S.-Y., J. Dudhia, and S.-H. Chen (2004), A revised approach to ice microphysical processes for the bulk parameterization, *Mon. Wea. Rev.*, *132*, 103–120.

Houze, R. A., Jr. (1993), *Cloud Dynamics*, 573 pp., Academic Press, San Diego.

Houze, R. A., Jr. (1997), Stratiform precipitation in regions of convection: A meteorological paradox?, *Bull. Amer. Meteor. Soc.*, *78*, 2179–2196.

Iguchi, T., T. Matsui, J.-J. Shi, W.-K. Tao, A. P. Khain, A. Hou, R. Cifelli, A. Heymsfield, and A. Tokay (2012), Numerical analysis using WRF-SBM for the cloud microphysical structures of the two distinct snowfall events during the C3VP field campaign, *J. Geophys. Res.*, *117*, D23206, doi:10.1029/2012JD018101.

Johnson, R. H., and P. J. Hamilton (1988), The relationship of surface pressure features to the precipitation and air flow structure of an intense midlatitude squall line, *Mon. Wea. Rev.*, *116*, 1444–1472.

Johnson, R. H., S. Chen, and J. J. Toth (1989), Circulations associated with a mature-to-decaying midlatitude mesoscale convective system. Part I: Surface features—Heat bursts and mesolow development, *Mon. Wea. Rev.*, *117*, 942–959.

Kumar, S. V., et al. (2006), LIS—An interoperable framework for high resolution land surface modeling, *Environ. Modell. Softw.*, *21*, 1402–1415.

Kumar, S. V., C. D. Peters-Lidard, J. L. Eastman, and W.-K. Tao (2007), An integrated high resolution hydrometeorological modeling testbed using LIS and WRF, *Environmental Modeling and Software*, *23*, 169–181.

Lafore, J.-P., and M. W. Moncrieff (1989), A numerical investigation of the scale interaction between a tropical squall line and its environment, *J. Atmos. Sci.*, *46*, 521–544.

Lang, S., W.-K. Tao, J. Simpson, and B. Ferrier (2003), Modeling of convective-stratiform precipitation processes: Sensitivity to partitioning methods, *J. Appl. Meteor.*, *42*, 505–527.

Lang, S., W.-K. Tao, R. Cifelli, W. Olson, J. Halverson, S. Rutledge, and J. Simpson, (2007), Improving simulations of convective system from TRMM LBA: Easterly and Westerly regimes, *J. Atmos. Sci.*, *64*, 1141–1164.

Lang, S., W.-K. Tao, X. Zeng, and Y. Li (2011), Reducing the biases in simulated radar reflectivities from a bulk microphysics scheme: Tropical convective systems, *J. Atmos. Sci.*, *68*, 2306–2320.

Lee, M. I., S. D. Schubert, M. J. Suarez, I. M. Held, N. C. Lau, J. J. Ploshay, A. Kumar, H. K. Kim, and J. K. E. Schemm (2007), An analysis of the warm-season diurnal cycle over the continental United States and northern Mexico in general circulation models, *J. Hydrometeorol.*, *8*, 344–366.

Lee, M.-I., I. Choi, W.-K. Tao, S. D. Schubert, and I.-K. Kang (2010), Mechanisms of diurnal precipitation over the United States Great Plains: A cloud-resolving model simulation, *Clim. Dyn.*, *34*, 419–437.

Liang, X.-Z., L. Li, A. Dai, and K. E. Kunkel (2004), Regional climate model simulation of summer precipitation diurnal cycle over the United States, *Geophy. Res. Lett.*, *31*, L24208, doi:10.1029/2004GL021054.

Liu, C., and M. W. Moncrieff (1998), A numerical study of the diurnal cycle of tropical oceanic convection, *J. Atmos. Sci.*, *55*, 2329–2344.

Liu, C., and M. W. Moncrieff (2007), Sensitivity of cloud-resolving simulations of warm-season convection to cloud microphysics parameterizations, *Mon. Wea. Rev.*, *135*, 2854–2868.

Liu, C.-H., M. W. Moncrieff, J. D. Tuttle, and R. E. Carbone (2006), Explicit and parameterized episodes of warm-season precipitation over the continental United States, *Adv. Atmos. Sci.*, *23*, 91–105.

Matsui, T., X. Zeng, W.-K. Tao, H. Masunaga, W. Olson, and S. Lang (2009), Evaluation of long-term cloud-resolving model simulations using satellite radiance observations and multifrequency satellite simulators, *J. Atmos. Oceanic Tech.*, *26*, 1261–1274.

Matsui, T., D. Mocko, M.-I. Lee, J. Chern, and W.-K. Tao (2010), Ten-year climatology of summertime diurnal rainfall rate over the Conterminous U.S, *Geophy. Res. Letter*, *37*, L13807, doi:10.1029/2010GL044139.

Mellor, G. L., and T. Yamada (1982), Development of a turbulence closure model for geophysical fluid problems, *Rev. Geophys. Space Phys.*, *20*, 851–875.

Meng, Z., F. Zhang, P. Markowski, D. Wu, and K. Zhao (2012), A modeling study on the development of a bowing structure and associated rear inflow within a squall line over south China, *J. Atmos. Sci.*, *69*, 1182–1207.

Moncrieff, M. W., and C. Liu (2006), Representing convective organization in prediction models by a hybrid strategy, *J. Atmos. Sci.*, *63*, 3404–3420.

Morrison, H., J. A. Curry, M. D. Shure, and P. Zuidema, (2005), A new double-moment microphysics parameterization for application in cloud and climate models. Part II: Single-column modeling of arctic clouds, *J. Atmos. Sci.*, *62*, 1678–1692.

Parker, M. D., and D. A. Ahijevych (2007), Convective episodes in the east-central United States, *Mon. Wea. Rev.*, *135*, 3707–3727.

Petersen, W. A., and M. Jensen (2012), The NASA-GPM and DOE-ARM Midlatitude Continental Convective Clouds Experiment (MC3E), *Int J Appl Earth Obs.*, *24*, 12–18, http://pmm.nasa.gov/sites/default/files/document_files/Earth_Observer_Jan_2012_MC3E.pdf.

Pielke, R. A., Sr. (2001), Influence of the spatial distribution of vegetation and soils on the prediction of cumulus convective rainfall, *Rev. Geophys.*, *39*, 151–177.

Putman, W. M., and M. Suarez (2011), Cloud-system resolving simulations with the NASA Goddard earth observing system global atmospheric model (GEOS-5), *Geophys. Res. Lett.*, *38*, L16809, doi:10.1029/2011GL048438.

Rotunno, R., J. B. Klemp, and M. L. Weisman (1988), A theory for strong, long-lived squall lines, *J. Atmos. Sci.*, *45*, 463–485.

Rutledge, S. A., R. A. Houze, Jr., and M. I. Biggerstaff (1988), The Olkahoma-Kansas mesoscale convective system of 10–11 June 1985: Precipitation structure and single-doppler radar analysis, *Mon. Wea. Rev.*, *116*, 1409–1430.

Santanello, J. A., Jr., C. D. Peters-Lidard, S. V. Kummar, C. Alonge, and W.-K. Tao (2009), A modeling and observational framework for diagnosing local land-atmosphere coupling on diurnal time scales, *J. Hydrometeorol.*, *10*, 577–599.

Satoh, M., T. Matsuno, H. Tomita, H. Miura, T. Nasuno, S. Iga (2008), Nonhydrostatic icosahedral atmospheric model (NICAM) for global cloud resolving simulations, *Journal of Computational Physics, the Special Issue on Predicting Weather*, *Clim. Extreme Events*, *227*, 3486–3514, doi:10.1016/J.JCP.2007.02.006.

Shi, J. J., W.-K. Tao, T. Matsui, A. Hou, S. Lang, C. Peters-Lidard, G. Jackson, R. Cifelli, S. Rutledge, and W. Petersen (2010), Microphysical properties of the January 20–22 2007 snow events over Canada: Comparison with in-situ and satellite observations, *J. Appl. Meteor. Climatol.*, *49*, 2246–2266.

Sui, C.-H., X. Li, and K.-M. Lau (1998), Radiative-convective processes in simulated diurnal variations of tropical oceanic convection, *J. Atmos. Sci.*, *55*, 2345–2359.

Surcel, M., M. Berenguer, and I. Zawadzki (2010), The diurnal cycle of precipitation from continental radar mosaics and numerical weather prediction models. Part I: Methodology and seasonal comparison, *Mon. Wea. Rev.*, *138*, 3084–3106, doi:10.1175/2010MWR3125.1.

Tao, W.-K., J. Simpson, C.-H. Sui, B. Ferrier, S. Lang, J. Scala, M.-D. Chou, and K. Pickering (1993), Heating, moisture and water budgets of tropical and midlatitude squall lines: Comparisons and sensitivity to long wave radiation., *J. Atmos. Sci.*, *50*, 673–690.

Tao, W.-K. (2003), Goddard cumulus ensemble (GCE) model: Application for understanding precipitation processes. *Cloud Systems*, *Hurricanes*, *and the Tropical Rainfall Measuring Mission* (*TRMM*): *A Tribute to Dr. Joanne Simpson*, *Meteor. Monogr.*, *51*, *Amer. Meteor. Soc*, 107–138.

Tao, W.-K., and M. Moncrieff (2009), Multiscale cloud-system modeling, *Rev. Geophys.*, *47*, RG4002, doi:10.1029/2008RG000276.

Tao, W.-K., and J. Simpson (1989), Modeling study of a tropical squall-type convective line, *J. Atmos. Sci.*, *46*, 177–202.

Tao, W.-K., and J. Simpson, and S.-T. Soong (1991), Numerical simulation of a sub-tropical squall line over Taiwan Strait, *Mon. Wea. Rev.*, *119*, 2699–2723.

Tao, W.-K., S. Lang, J. Simpson, C.-H. Sui, B. Ferrier, and M.-D. Chou (1996), Mechanisms of cloud-radiation interaction in the Tropics and midlatitudes, *J. Atmos. Sci.*, *53*, 2624–2651.

Tao, W.-K., J. J. Shi, S. S. Chen, S. Lang, P.-L. Lin, S.-Y. Hong, C. Perters-Lidard, and A. Hou (2011a), The impact of microphysical schemes on hurricane intensity and track, *Asia-Pac. J. Atmos. Sci.*, *47*, 1–16.

Tao, W.-K., et al. (2011b), High resolution numerical simulation of the extreme rainfall associated with Typhoon Morakot. Part I: Impact of microphysics and PBL, *Terr. Atmos. Ocean. Sci.*, *22*, 6, 673–696, doi:10.3319/TAO2011.08.26.01.

Trier, S. B., C. A. Davis, D. A. Ahijevych, M. L. Weisman, and G. H. Bryan (2006), Mechanisms supporting long-lived episodes of propagating nocturnal convection within a 7-day WRF model simulation, *J. Atmos. Sci.*, *63*, 2437–2461.

Trier, S. B., C. A. Davis, and D. A. Ahijevych (2010), Environmental controls on the simulated diurnal cycle of warm-season precipitation in the continental United States, *J. Atmos. Sci.*, *67*, 1066–1090.

Trier, S. B., J. H. Marsham, C. A. Davis, and D. A. Ahijevych (2011), Numerical simulations of the postsunrise recorganization of a nocturnal mesoscale convective system during 13 June IHOP_2002, *J. Atmos. Sci.*, *68*, 2988–3011.

Tripoli, G. J., and W. R. Cotton (1989a), Numerical study of an observed orogenic mesoscale convective system. Part 1: Simulated genesis and comparison with observations, *Mon. Wea. Rev.*, *117*, 273–304.

Tripoli, G. J., and W. R. Cotton (1989b), Numerical study of an observed orogenic mesoscale convective system. Part 2: Analysis of governing dynamics, *Mon. Wea. Rev.*, *117*, 305–328.

Wakimoto, R. M. (1982), The life cycle of thunderstorm gust fronts as viewed with Doppler radar and rawinsonde data, *Mon. Wea. Rev.*, *110*, 1060–1082.

Wallace, J. M. (1975), Diurnal variations in precipitation and thunderstorm frequency over the conterminous United States, *Mon. Wea. Rev*, *103*, 406–419.

Weisman, M. L., B. Klemp, and R. Rotunno, (1988), Structure and evolution of numerically simulated squall lines, *J. Atmos. Sci.*, *45*, 1990–2013.

Xu, K.-M., and D. A. Randall (1995), Impact of interactive radiative transfer on the microscopic behavior of cumulus ensembles. Part II: Mechanisms for cloud-radiation interactions, *J. Atmos. Sci.*, *52*, 800–817.

Yuter, S. E., and R. A. Houze, Jr. (1995), Three-dimensional kinematic and microphysical evolution of Florida cumulonimbus. Part II: Frequency distribution of vertical velocity, reflectivity, and differential reflectivity, *Mon. Wea. Rev.*, *123*, 1941–1962.

Zhang, J., K. Howard, and J. J. Gourley (2005), Constructing three dimensional multiple-radar reflectivity mosaics: Examples of convective storms and stratiform rain echoes, *J. Atmos. Oceanic Technol.*, *22*, 30–42, doi:10.1175/JTECH-1689.1.